ACS NANO

Open Access

www.acsnano.org

ARTICLE

An Engineered Bionic Nanoparticle Sponge as a Cytokine Trap and Reactive Oxygen Species Scavenger to Relieve Disc Degeneration and Discogenic Pain

Wenbo Yang,[#] Kanglu Li,[#] Qing Pan,[#] Wei Huang, Yan Xiao, Hui Lin, Sheng Liu, Xuanzuo Chen, Xiao Lv, Shiqing Feng, Zengwu Shao,* Xiangcheng Qing,* and Yizhong Peng*

Cite This: *ACS Nano* 2024, 18, 3053−3072

Read Online

ACCESS | Metrics & More | Article Recommendations | Supporting Information

ABSTRACT: **The progressive worsening of disc degeneration and related nonspecific back pain are prominent clinical issues that cause a tremendous economic burden. Activation of reactive oxygen species (ROS) related inflammation is a primary pathophysiologic change in degenerative disc lesions. This pathological state is associated with M1 macrophages, apoptosis of nucleus pulposus cells (NPC), and the ingrowth of pain-related sensory nerves. To address the pathological issues of disc degeneration and discogenic pain, we developed MnO_2@TMNP, a nanomaterial that encapsulated MnO_2 nanoparticles with a TrkA-overexpressed macrophage cell membrane (TMNP). Consequently, this engineered nanomaterial showed high efficiency in binding various inflammatory factors and nerve growth factors, which inhibited inflammation-induced NPC apoptosis, matrix degradation, and nerve ingrowth. Furthermore, the macrophage cell membrane provided specific targeting to macrophages for the delivery of MnO_2 nanoparticles. MnO_2 nanoparticles in macrophages effectively scavenged intracellular ROS and prevented M1 polarization. Supportively, we found that MnO_2@TMNP prevented disc inflammation and promoted matrix regeneration, leading to downregulated disc degenerative grades in the rat injured disc model. Both mechanical and thermal hyperalgesia were alleviated by MnO_2@TMNP, which was attributed to the reduced calcitonin gene-related peptide (CGRP) and substance P expression in the dorsal root ganglion and the downregulated Glial Fibrillary Acidic Protein (GFAP) and Fos Proto-Oncogene (c-FOS) signaling in the spinal cord. We confirmed that the MnO_2@TMNP nanomaterial alleviated the inflammatory immune microenvironment of intervertebral discs and the progression of disc degeneration, resulting in relieved discogenic pain.**

KEYWORDS: *biomembrane-coated nanoparticles, cytokine trap, ROS scavenger, disc degeneration, discogenic pain*

INTRODUCTION

Low back pain (LBP) is a major clinical and socioeconomic health burden worldwide.[1] The prevalence of LBP has been reported to be near 30%, with a lifetime prevalence of over 80%.[2,3] LBP can be divided into specific pain with a clear cause (e.g., due to disc herniation and anatomical changes) and nonspecific pain (the exact cause is unknown).[4] Treatment of nonspecific LBP is complex, because the pathogenesis is not clear. It has been suggested that intervertebral disc degeneration (IDD) may be a major cause of nonspecific pain in patients with LBP, also known as discogenic low back pain.[5] Discogenic low back pain is considered as a sign of IDD. Discogenic low back pain is not an indication for spinal surgery, and treatment of discogenic pain is mostly based on symptomatic supportive therapy.[6] However, it is worth noting that the symptoms of many patients with discogenic back pain progressively worsen and eventually develop specific pain because the pathological state of the disc microenvironment is not effectively altered by traditional treatment.[7] Patients may eventually undergo an invasive treatment or open surgery to relieve their pain. Therefore, how to effectively relieve discogenic back pain and restrict disease progression is an urgent clinical problem.

The pathological state of the local microenvironment of the intervertebral disc (IVD) is a key factor contributing to increased IDD and discogenic back pain.[8] Macrophages are

Received: August 27, 2023
Revised: December 28, 2023
Accepted: January 3, 2024
Published: January 18, 2024

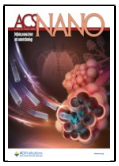

https://doi.org/10.1021/acsnano.3c08097
ACS Nano 2024, 18, 3053−3072

Scheme 1. Synthesis and Biological Mechanism of MnO_2@TMNP[a]

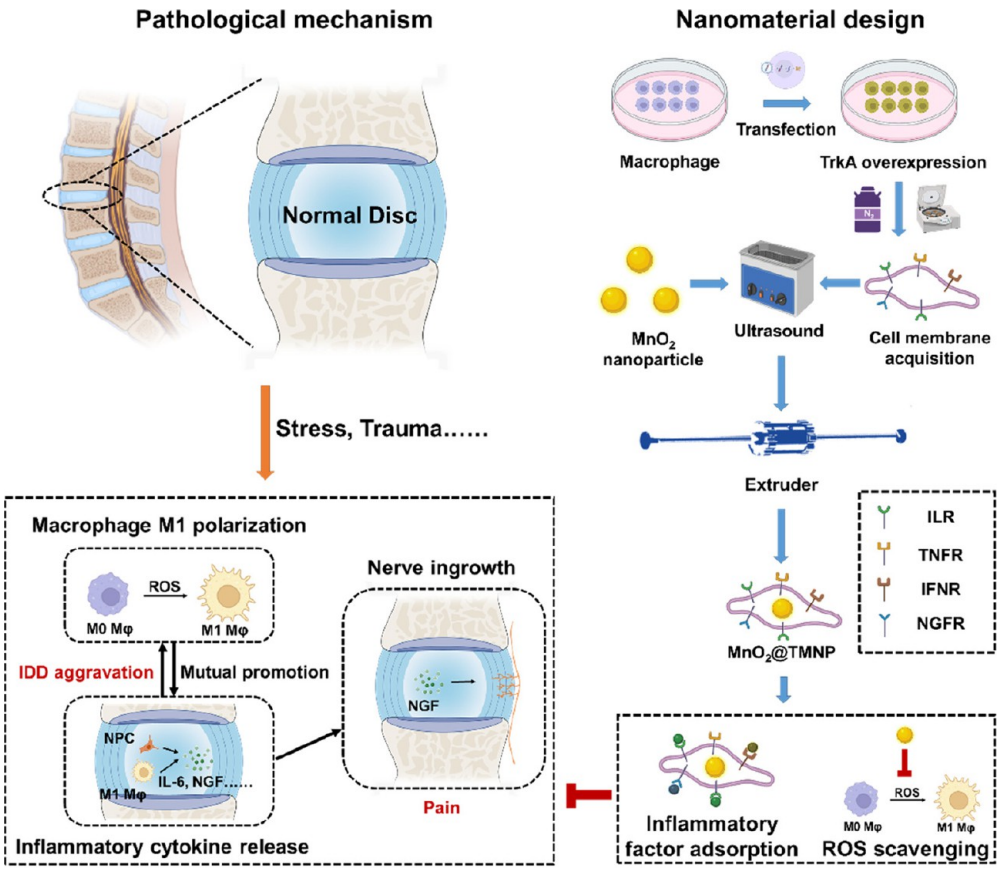

[a]MnO_2 nanoparticles coated with TrkA-overexpressed macrophage membranes (MnO_2@TMNP) inhibit M1 polarization by extensively scavenging ROS and decoying proinflammatory cytokines and NGF, ultimately alleviating the progression of disc degeneration and discogenic back pain. Abbreviations: Mφ, macrophage; NGF, nerve growth factor; ROS, reactive oxygen species; ILR, interleukin receptors; TNFR, tumor necrosis factor receptors; IFNR, interferon receptors; NGFR, nerve growth factor receptors (TrkA in this study).

able to infiltrate into the nucleus pulposus and manifest as M1 type macrophages, contributing to the development of disease.[9] The number of M1 macrophages is positively correlated with the chronic inflammation of IDD.[10] It has been shown that in degenerating discs, M1-type macrophages create a chronic inflammatory microenvironment by releasing inflammatory factors such as interleukin-6 (IL-6), tumor necrosis factor-α (TNF-α), and interleukin-1β (IL-1β).[11] This persistent state of immune activation exacerbates disc destruction, and M1 macrophages in the pathological microenvironment are considered to be some of the enforcers of the IDD mechanism.[12]

Additionally, M1-type macrophages and the chronic inflammatory microenvironment are thought to be critical in the development of nerve ingrowth and painful signaling activation.[13−15] The chronic inflammatory microenvironment induces sensory nerve growth as well as sensitivity, leading to the development of discogenic pain.[16] The sensory nerves innervating the disc originating from small dorsal root ganglion (DRG) neurons consist mainly of nerve growth factor (NGF) dependent and glial cell line derived neurotrophic factor (GDNF) dependent nerves.[17] These nerves are generally located in the outer layer of the annulus fibrous (AF) and the area among the end plates.[18] In the pathological chronic inflammation microenvironment, inflammatory cytokines such as IL-1β and TNF-α released by M1 macrophages stimulate the production of NGF, and the sustained release of NGF leads to innervation into the degenerating disc, resulting in sensitization of peripheral afferent nerves, which is a significant cause of discogenic low back pain.[19,20] Therefore, avoiding M1 macrophage polarization and removing the residual inflammatory factors and NGF in the microenvironment is the key issue in delaying the progression of IDD and relieving discogenic pain.

Reactive oxygen species (ROS) play an important role in M1 macrophage polarization.[14,21] It has been shown that ROS levels are elevated in degenerating disc tissue.[22] Increased ROS induce M1 polarization of macrophages through various mechanisms, such as affecting the MAPK pathway, etc.[21] The polarized M1 macrophages sequentially produce more ROS, creating an undesirable cycle that promotes the progression of disc degeneration.[23] Therefore, removing the excess ROS in macrophages may be a feasible approach to alleviating disc degeneration. In recent years, many nanoparticles have been developed as ROS scavengers, especially certain metal-containing nanoparticles.[24] MnO_2 nanoparticles are an ideal choice for in vivo ROS scavengers due to their broad antioxidant activity.[25] MnO_2 nanoparticles phagocytosed by cells often exhibit enzymatic effects similar to those of ROS-scavenging enzymes, such as superoxide dismutase (SOD).[26] Therefore, MnO_2 nanoparticles may block macrophage polarization toward M1 in the degenerative disc microenvironment as an efficient ROS scavenger. However, MnO_2 nanoparticles lack macrophage targeting, which may limit the cellular uptake and function of the MnO_2 nanoparticles. Thus, further modification of the MnO_2

https://doi.org/10.1021/acsnano.3c08097
ACS Nano 2024, 18, 3053−3072

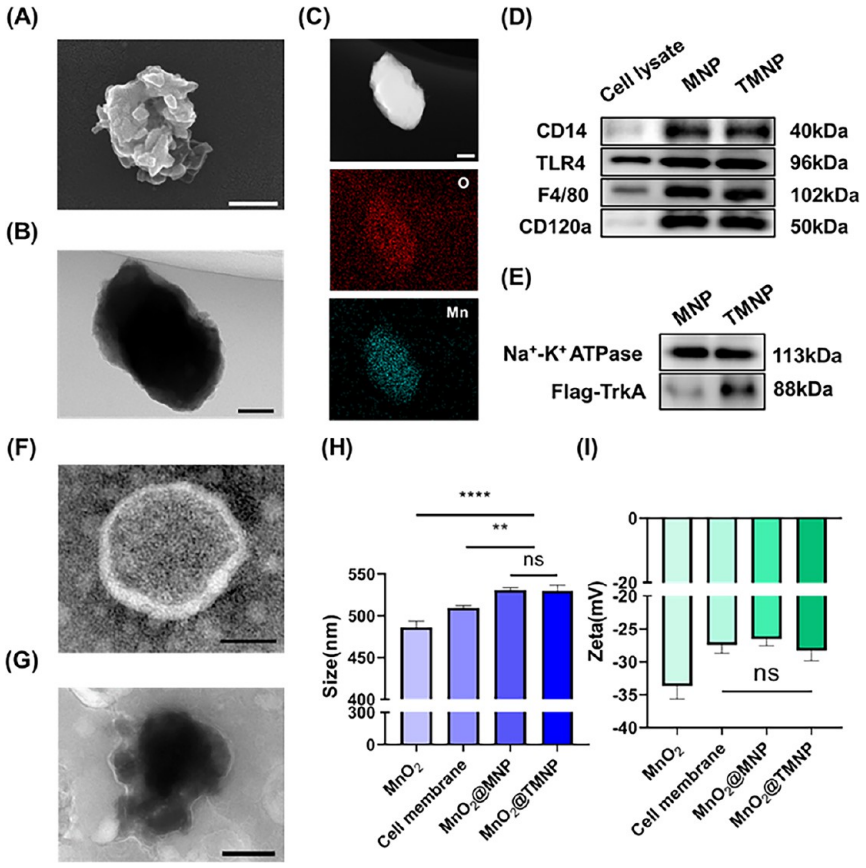

Figure 1. Characterization of the nanomaterials. (A) SEM of the MnO_2 nanoparticles. Scale bar: 200 nm. (B) TEM image of MnO_2 nanoparticles. Scale bar: 100 nm. (C) HAADF and mapping results of MnO_2 nanoparticles. Scale bar: 100 nm. (D) Western blot analysis of CD14, TLR4, F4/80, and CD120a on the membrane of the nanomaterial. (E) Western blot analysis of TrkA on the membrane of the nanomaterial. TEM images of macrophage membrane vesicles (TMNP) (F) and MnO_2@TMNP (G). Scale bars: 200 nm. (H) Comparison of particle sizes of MnO_2 nanoparticles, cell membrane vesicles, MnO_2@MNP, and MnO_2@TMNP. (I) Comparison of zeta potentials of MnO_2 nanoparticles, cell membrane vesicles, MnO_2@MNP, and MnO_2@TMNP. Data are presented as the mean ± SD (n = 3): ns, not significant; **, p < 0.01; ****, p < 0.0001 between groups.

nanoparticles is required to provide them with macrophage targeting properties.

Cell membrane encapsulation, derived from the concept of bionanotechnology, involves disguising nanoparticles as "vesicles" to achieve active targeting with a high efficiency toward specific cells.[27] Biological membrane-encapsulated nanomaterials, such as tumor or hybrid cell membranes, exhibit a high specificity toward target cells of the relative type.[28,29] Macrophage membrane-encapsulated MnO_2 nanoparticles may present a promising strategy for selectively scavenging excessive ROS in macrophages. Besides, macrophages express receptors for various cellular inflammatory factors, such as IL-1 and IL-6 receptors on their cell membrane surfaces.[30−32] These receptors on macrophage membranes enable efficient binding to inflammatory cytokines, thereby facilitating the role of macrophage membranes as "molecular sponges" that decoy inflammatory factors and modulate the inflammatory immune microenvironment.[33] Enabling macrophage cell membranes to adsorb NGF is the key to alleviating discogenic pain caused by nanomaterials. TrkA, a transmembrane protein, serves as a specific receptor for NGF.[34] Therefore, it is feasible to engineer cell membranes with a high expression of TrkA as "molecular sponges" for capturing NGF.

In this study, we innovatively employed macrophage membranes with high TrkA expression to encapsulate MnO_2 nanoparticles as ROS scavengers (MnO_2@TMNP) for the treatment of IDD. MnO_2@TMNP has the potential to decoy inflammatory cytokines and NGF while selectively targeting macrophages to remove excess ROS and prevent M1-type polarization of macrophages, which may delay the progression of disc degeneration and the onset of pain. The design concept and action mechanism are illustrated in Scheme 1.

RESULTS

Preparation and Characterization of Materials. To achieve the specific targeting of immune cells, ROS clearance, and the adsorption of inflammatory factors, we developed functionalized nanoparticles with MnO_2 nanoparticles as the core encapsulated in an engineered macrophage membrane (Scheme 1). The SEM results of the MnO_2 nanoparticles are shown in Figure 1A. The size of the nanoparticles was about 400−500 nm, and the surface was polymorphic. The irregular morphology of the nanoparticles provided a larger specific surface area than the same volume spherical MnO_2 nanoparticles for possible efficient catalysis of the decomposition of ROS components.[35] Through TEM and elemental analysis, we not only ascertained that the nanomaterial possessed a solid and irregular structure but also confirmed the chemical composition of the nanomaterial (Figure 1B,C). Subsequently, we endeavored to coat the MnO_2 nanoparticles with macrophage cell

https://doi.org/10.1021/acsnano.3c08097
ACS Nano 2024, 18, 3053−3072

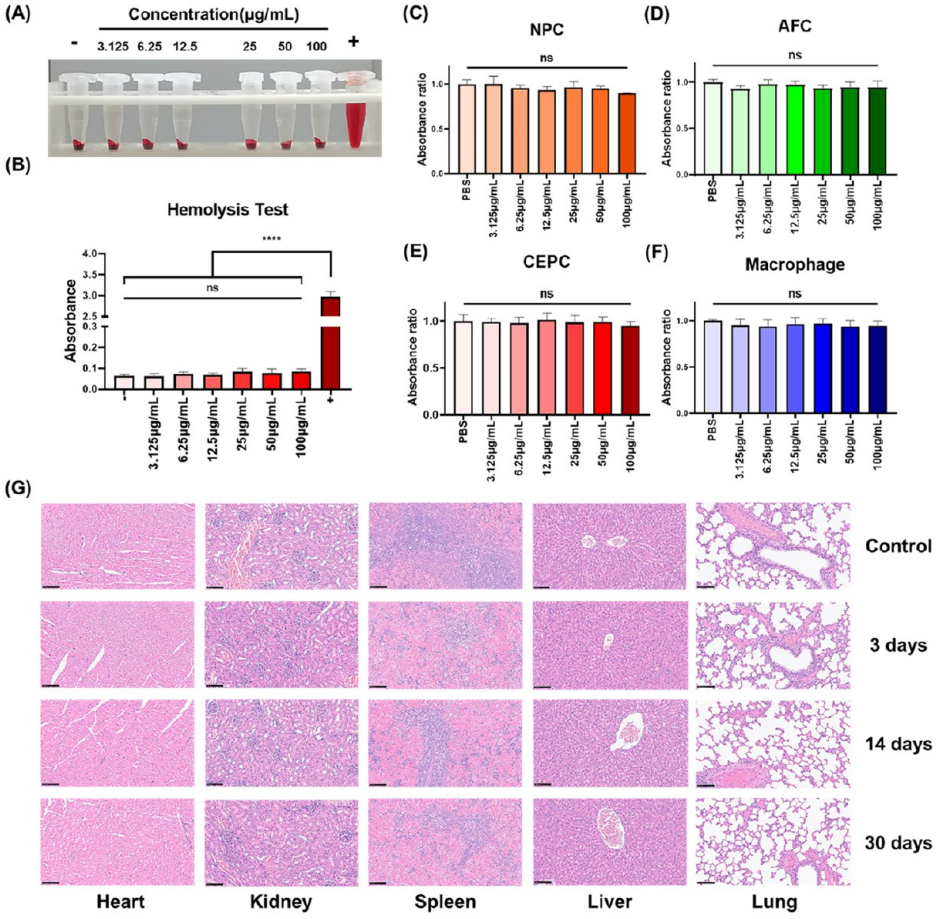

Figure 2. Biosafety of MnO_2@TMNP nanomaterials. (A) Hemolysis assay of MnO_2@TMNP cocultured with rat blood cells. (B) Absorbance test at 541 nm of the supernatant obtained by centrifugation after coculture of MnO_2@TMNP and red blood cells. Cell viability after MnO_2@TMNP cocultured with nucleus pulposus cells (NPC) (C), annulus fibrosus cells (AFC) (D), cartilage end plate cells (CEPC) (E), and macrophages (F). (G) Histological morphological observation of major organs at different time periods after the injection of MnO_2@TMNP into the rat tail vein. Scale bars: 100 μm. Data are presented as the mean ± SD (n = 3): ns, not significant; ****, $p < 0.0001$ between groups.

membranes overexpressing TrkA. Western blot experiments confirmed that the extracted cell membranes exhibited a high expression of CD14, CD120a, F4/80, TLR4, and TrkA, consistent with macrophage cells overexpressing TrkA (Figure 1D,E and Figure S1). The negative TEM of individual cell membrane vesicles, as illustrated in Figure 1F, confirmed the ability of the cellular membrane structure to produce appropriately sized vesicles upon pressure. Subsequently, MnO_2 nanoparticles were subjected to compression and amalgamation of the cell membrane via a compression apparatus, resulting in the formation of MnO_2@TMNP as depicted in Figure 1G. We observed a clear membrane-like structure on the surface of MnO_2@TMNP nanoparticles following extrusion (Figure 1G). The nanoparticle structure was further validated through particle size detection and zeta potential analysis (Figure 1H,I). Through particle size detection, we found that MnO_2@TMNP and MnO_2@MNP exhibited an increase of approximately 50 nm in particle size compared to that of the MnO_2 nanoparticles. The zeta potential of MnO_2@TMNP was similar to that of the cell membrane, indicating a successful membrane coating. The overexpression of TrkA did not significantly alter either the zeta potential or particle size. We also detected the protein distribution of different nanomaterials by SDS-PAGE and Coomassie bright blue staining, further confirming the success of membrane coating and the correctness of nanomaterial composition (Figure S2). We also confirm that the encapsulation rate of MnO_2 during the synthesis of MnO_2@TMNP is 84.7%.

Biosafety of MnO_2@TMNP Nanomaterials. To ensure the biocompatibility of MnO_2@TMNP, we conducted various biosafety studies. Hemolysis assays demonstrated that even at a concentration of 100 μg/mL, MnO_2@TMNP did not induce significant erythrocyte lysis (Figure 2A,B), indicating that MnO_2@TMNP had no clear circulatory toxicity. Subsequently, various concentrations of MnO_2@TMNP were cocultured with IVD-related cells, including NPC, AFC, CEPC, and macrophages. Cell viability was assessed using the CCK-8 assay. Results showed that MnO_2@TMNP with different concentrations did not significantly affect cell viability (Figure 2C−F). Further, the nanomaterials were administered to rats, and HE staining was applied to their major organs. Subsequent observations of heart, liver, spleen, lungs, and kidneys confirmed that MnO_2@TMNP exhibited negligible organ toxicity (Figure 2G).

LPS, Inflammatory Factor, and NGF Capturing Ability of the Nanomaterials. As discussed before, the engineered cell membrane on the outer layer of the nanomaterial contained various receptors for inflammatory factors and NGF (TrkA), which may serve as a decoy to capture these molecules associated with nerve growth and pain. Therefore, we evaluate

https://doi.org/10.1021/acsnano.3c08097
ACS Nano 2024, 18, 3053−3072

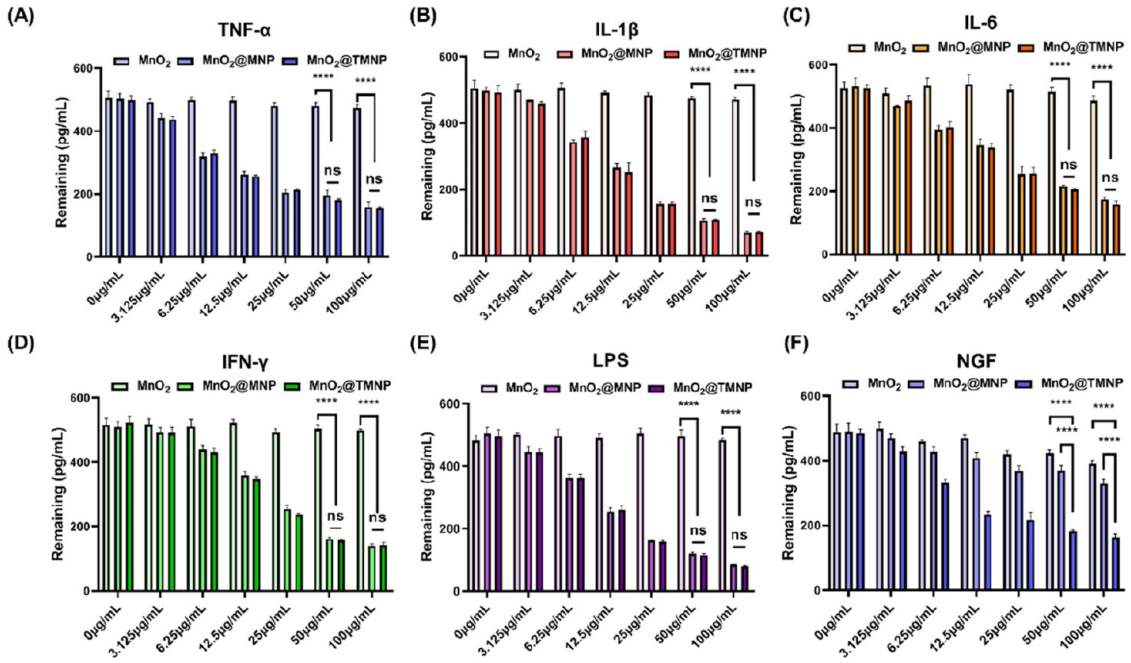

Figure 3. Validation of adsorption capacity of nanomaterials with different concentration gradients on inflammatory factors/LPS/NGF. The remaining concentrations of TNF-α (A), IL-1β (B), IL-6 (C), IFN-γ (D), LPS (E), and NGF (F) were detected by an enzyme-linked immunosorbent assay (ELISA), after coculturing with MnO_2 nanoparticles, MnO_2@MNP nanoparticles, and MnO_2@TMNP nanoparticles at different concentrations. The initial concentrations of cytokines, LPS and NGF were 500 pg/mL. Data are presented as the mean ± SD (n = 3): ns, not significant; ****, p < 0.0001 between groups.

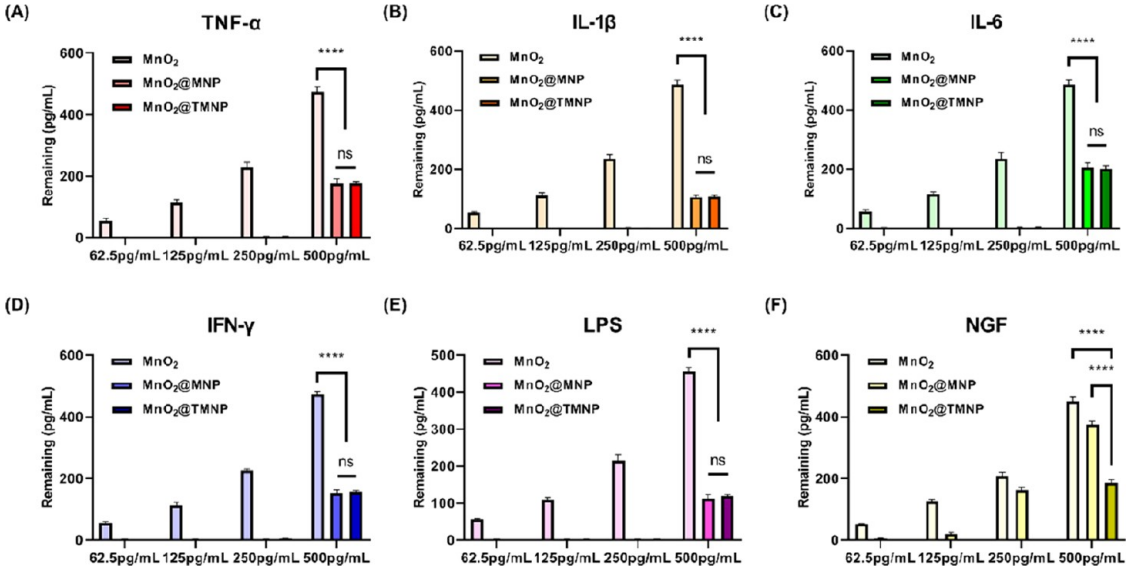

Figure 4. Validation of the adsorption capacity of fixed concentrations of nanomaterials to inflammatory cytokines/LPS/NGF with different concentration gradients. The remaining concentrations of TNF-α (A), IL-1β (B), IL-6 (C), IFN-γ (D), LPS (E), and NGF (F) at different initial concentrations were detected, after coculturing with 50 μg/mL MnO_2@TMNP. Data are presented as the mean ± SD (n = 3): ns, not significant; ****, p < 0.0001 between groups.

the ability of nanomaterials to bind LPS, various cytokines, including TNF-α, IL-1β, IL-6, IFN-γ, and NGF. After mixing the nanomaterials with these factors and incubating at 37 °C for 2 h, the nanomaterials were removed by ultracentrifugation and the remaining factors in solution were measured. We found that MnO_2 nanoparticles removed negligible LPS and cytokines, while both MnO_2@MNP and MnO_2@TMNP demonstrated significant binding capacities for these factors (Figure 3A–E). Moreover, with an increase in MnO_2@MNP and MnO_2@TMNP concentration, there was a significant decrease in the remaining inflammatory factor concentrations (Figure 3A–E). Consistent with our expectation, the remaining NGF significantly decreased only in the MnO_2@TMNP group as the concentration of nanomaterials increased (Figure 3F).

Concurrently, we altered the concentration of LPS and cytokines while controlling the concentration of MnO_2@TMNP to 50 μg/mL to further evaluate the binding efficiency of MnO_2@TMNP with respect to inflammatory factors (Figure

https://doi.org/10.1021/acsnano.3c08097
ACS Nano 2024, 18, 3053−3072

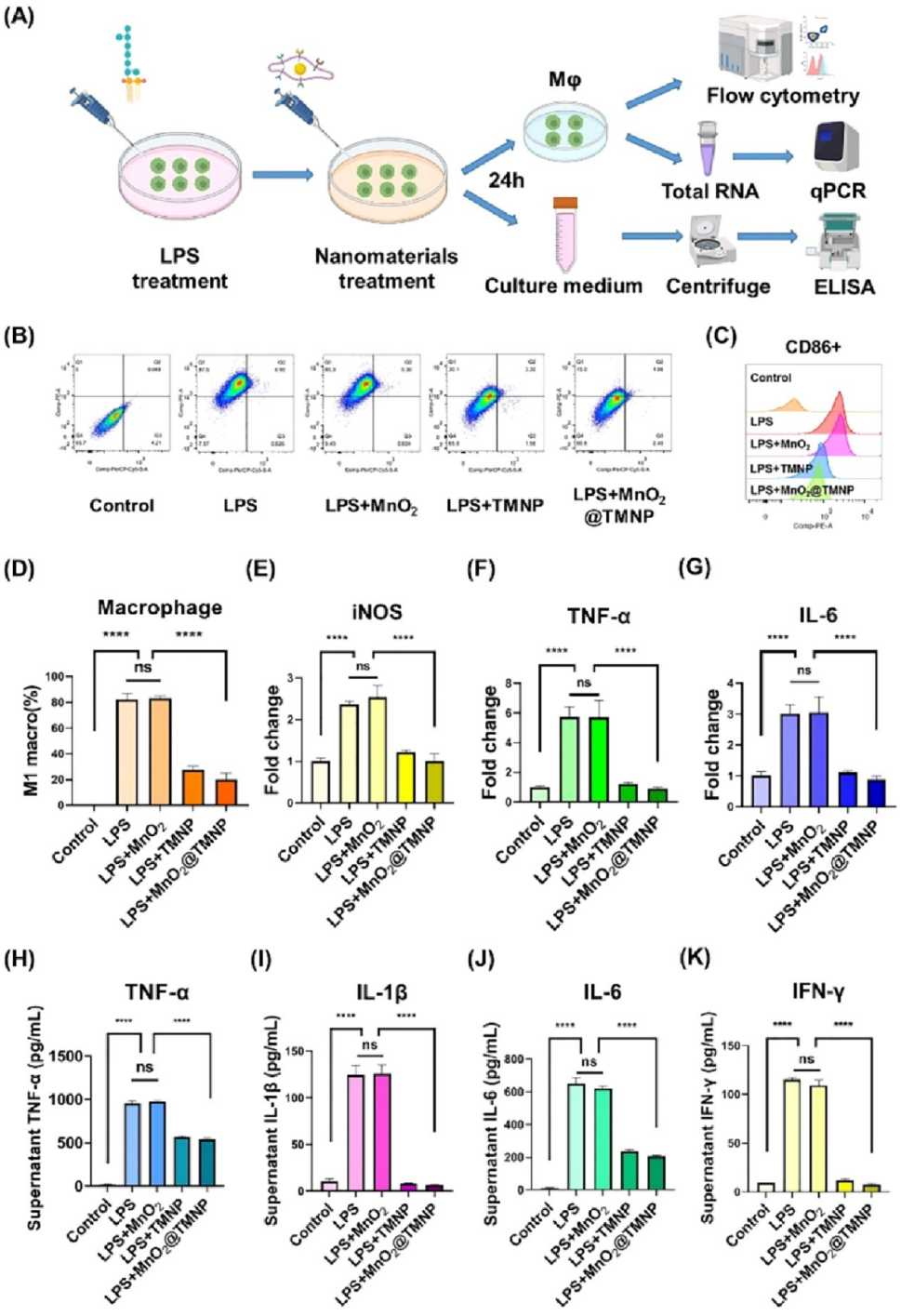

Figure 5. MnO_2@TMNP inhibits the LPS-induced M1 polarization of macrophages. (A) Schematic diagram of the experimental design. (B) Flow cytometry detecting F4/80+CD86+ cells and F4/80+CD206+ cells to evaluate the polarization of macrophages. (C) Quantification of the CD86 geomean fluorescence intensity of macrophages according to flow cytometry. (D) Quantification of the proportion of M1 macrophages in each group. The levels of mRNA encoding iNOS (E), TNF-α (F), and IL-6 (G) in macrophages treated with LPS, LPS+MnO_2, LPS+TMNP, or LPS+MnO_2@TMNP, respectively. The fold change was normalized to the control group. The concentrations of TNF-α (H), IL-1β (I), IL-6 (J), and IFN-γ (K) in the supernatant after treating macrophages with LPS, LPS+MnO_2, LPS+TMNP, or LPS+MnO_2@TMNP. Data are presented as the mean ± SD (n = 3): ns, not significant; ****, p < 0.0001 between groups.

4A−F). We found that when the concentration was below 250 pg/mL, nearly all of the LPS and cytokines were removed by MnO_2@TMNP. When the concentration reached 500 pg/mL, 30−40% of the LPS and cytokines remained in the solution. MnO_2 nanoparticles showed no effective adsorption of inflammatory cytokines/LPS/NGF, while only MnO_2@TMNP nanoparticles showed obvious adsorption of NGF. These results demonstrated the binding capacity of MnO_2@TMNP for inflammatory factors and NGF, which was attributed to the macrophage membrane overexpressing TrkA, indicating the potential application of MnO_2@TMNP in inflammation and pain elimination.

MnO_2@TMNP Prevents M1 Macrophage Polarization and Alleviates the Inflammatory Microenvironment.

https://doi.org/10.1021/acsnano.3c08097
ACS Nano 2024, 18, 3053−3072

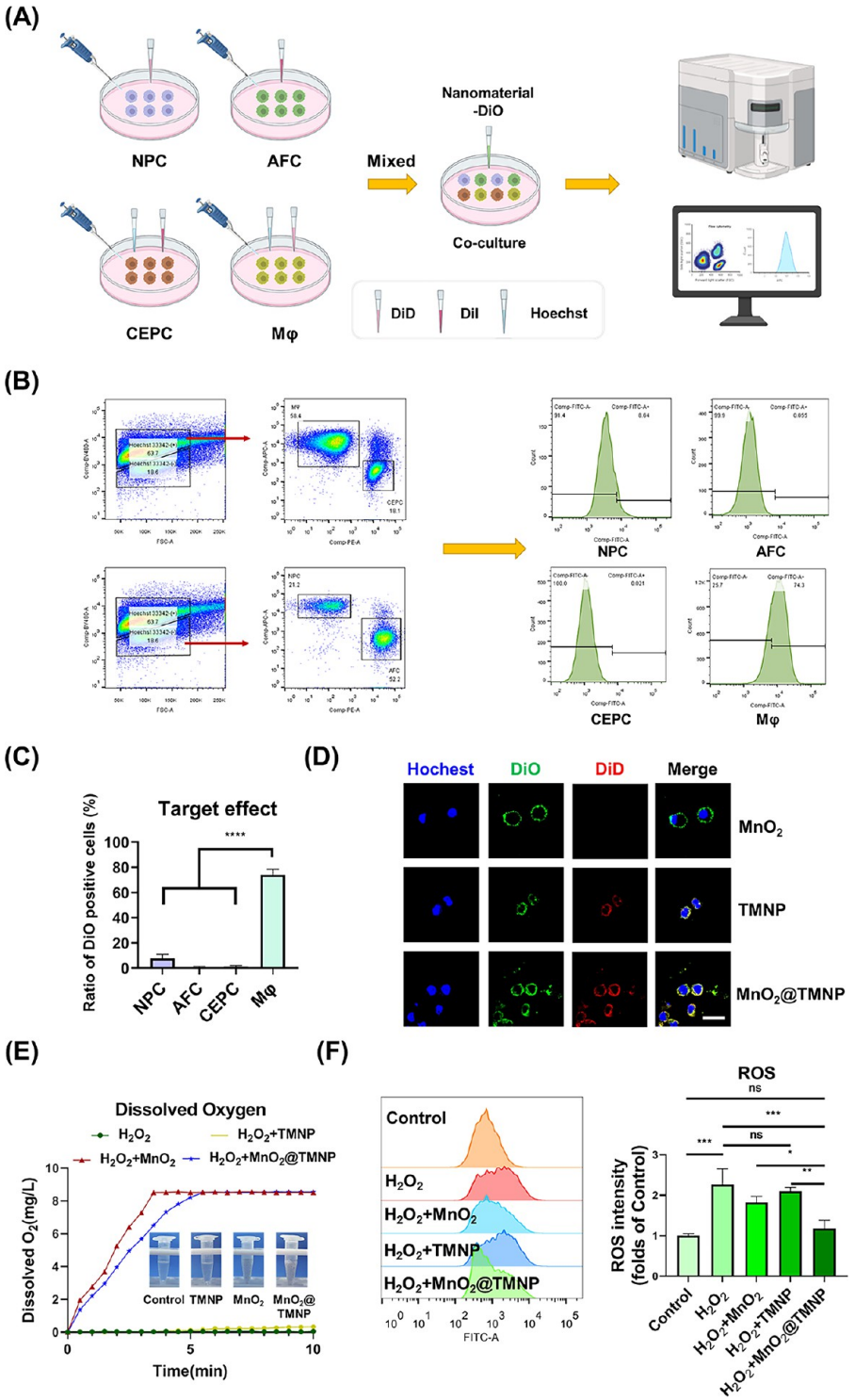

Figure 6. Ability of MnO_2@TMNP to specifically target macrophages for ROS clearance. (A) Flowchart for the evaluation of macrophages taking up nanoparticles. (B) Flow cytometry results of the uptake of DiO-loaded nanoparticles by different cells. (C) Statistical analysis of the positive DiO rate of different cells. (D) Fluorescence images of the fusion of DiD-loaded nanoparticles and DiO-loaded macrophages. Scale bar: 20 μm. (E) Records of dissolved oxygen in water to assess the H_2O_2 decomposition catalyzed by MnO_2@TMNP, MnO_2 nanoparticles, or TMNP. (F) Flow cytometry of intracellular ROS indicating the effects of MnO_2@TMNP, MnO_2 nanoparticles, or TMNP on scavenging ROS. The ROS intensity was normalized to the control group. Data are presented as the mean ± SD (n = 3): ns, not significant; *, $p < 0.05$; **, $p < 0.01$; ***, $p < 0.001$; ****, $p < 0.0001$ between groups.

After confirming the binding capacity of the macrophage membrane for LPS, the key regulator of M1 polarization, we further evaluated the capacity of MnO_2@TMNP for modulating the phenotype of macrophages. The schematic diagram of the experimental design is shown in Figure 5A. We initially supplemented the medium with 1 μg/mL LPS, followed by the immediate addition of PBS or different nanomaterials (50 μg/mL), with a subsequent incubation for 24 h before further

https://doi.org/10.1021/acsnano.3c08097
ACS Nano 2024, 18, 3053−3072

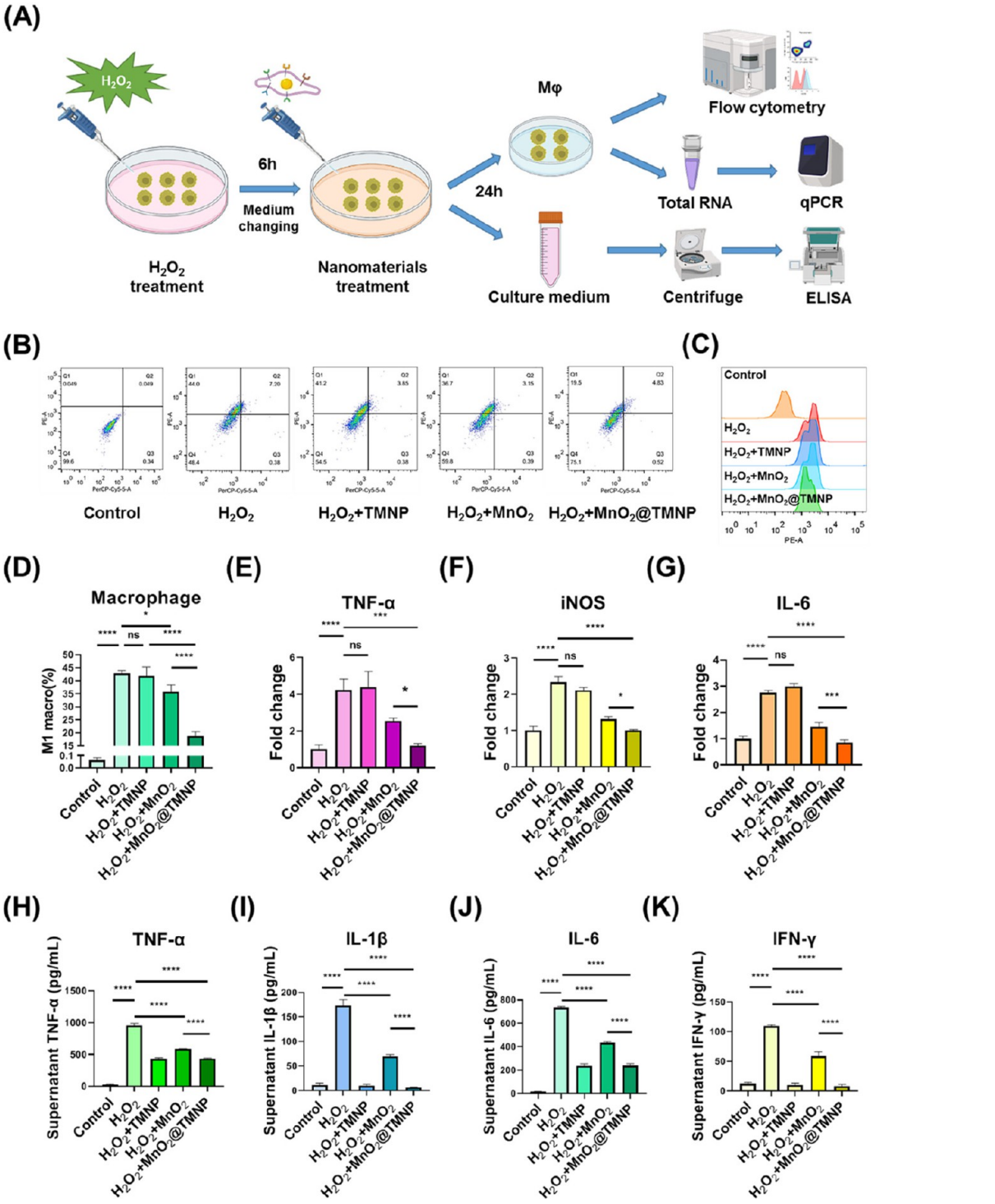

Figure 7. MnO_2@TMNP inhibits H_2O_2-induced M1 macrophage polarization. (A) Schematic illustration of the establishment of H_2O_2-induced macrophage M1 polarization to assess the effects of MnO_2@TMNP on alleviating the inflammatory microenvironment. (B) Flow cytometry of macrophage polarization after treatment with H_2O_2, H_2O_2+MnO_2, H_2O_2+TMNP, or H_2O_2+MnO_2@TMNP. (C) CD86 geomean fluorescence intensity of macrophages according to flow cytometry. (D) Quantification of the proportion of M1 macrophages in each group. The mRNA content of TNF-α (E), iNOS (F), and IL-6 (G) in macrophages treated with H_2O_2, H_2O_2+MnO_2, H_2O_2+TMNP, or H_2O_2+MnO_2@TMNP. The fold change was normalized to the control group. The concentrations of TNF-α (H), IL-1β (I), IL-6 (J), and IFN-γ (K) in the supernatant after treating macrophages with H_2O_2, H_2O_2+MnO_2, H_2O_2+TMNP, or H_2O_2+MnO_2@TMNP. Data are presented as the mean ± SD (n = 3): ns, not significant; *, $p < 0.05$; **, $p < 0.01$; ***, $p < 0.001$; ****, $p < 0.0001$ between groups.

evaluation. Flow cytometry analysis revealed that exposure to LPS increased the percentage of CD86+ macrophages, indicating the polarization of M0 macrophages toward the M1 phenotype, while MnO_2@MNP and MnO_2@TMNP, but not MnO_2 nanoparticles, effectively reversed this effect (Figure 5B–D). The PCR results suggested that coculturing macrophages with LPS led to a significant upregulation of M1-type polarization markers (Figure 5E–G). The upregulation of M1

https://doi.org/10.1021/acsnano.3c08097
ACS Nano 2024, 18, 3053–3072

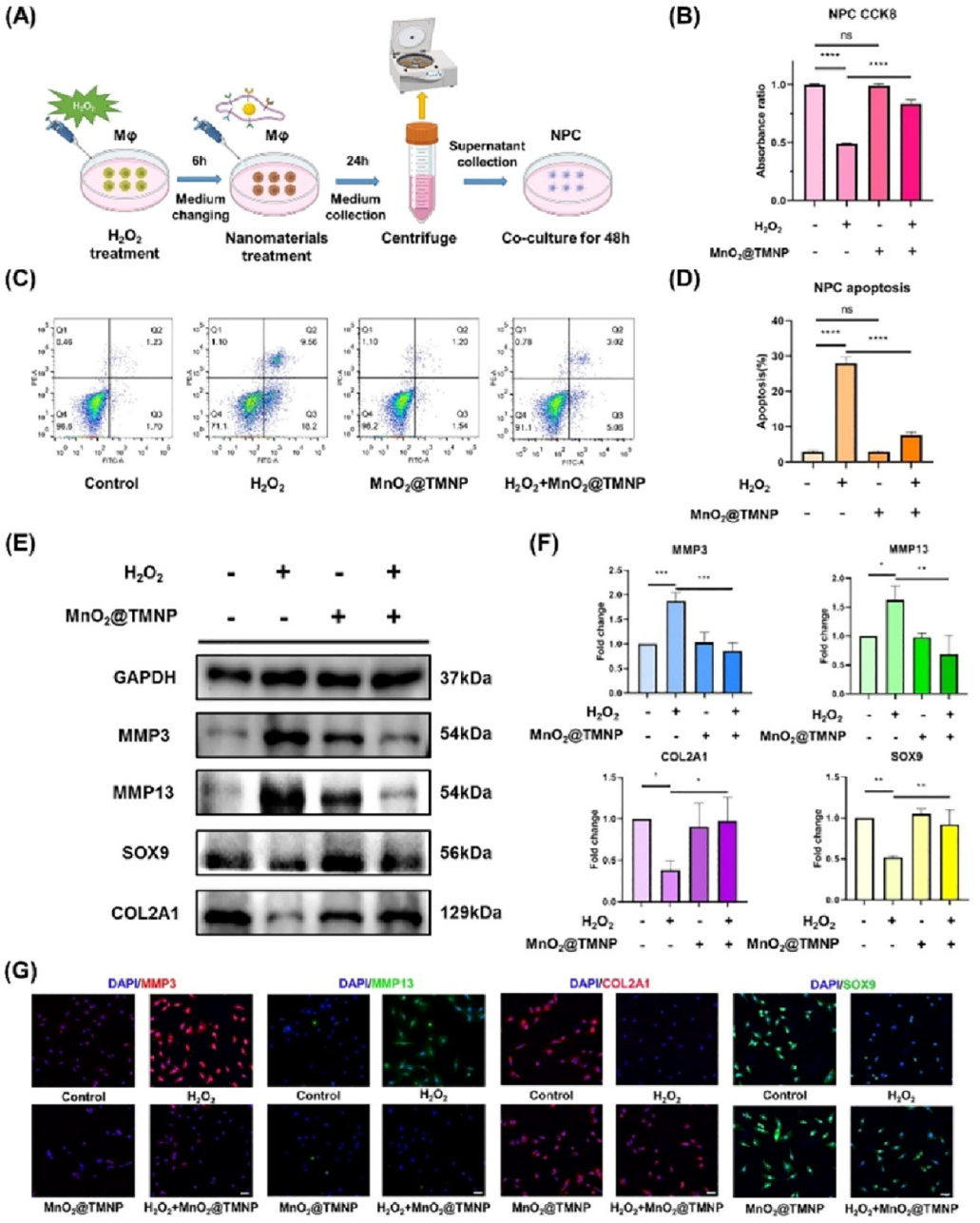

Figure 8. MnO_2@TMNP alleviated cell death and matrix degradation in a proinflammatory microenvironment. (A) Schematic illustration of the establishment of an inflammatory microenvironment for NPCs to evaluate the protective effects of MnO_2@TMNP. (B) Viability of NPCs treated by supernatant extracted from macrophages that had been treated with H_2O_2, MnO_2@TMNP, or a combination of H_2O_2 and MnO_2@TMNP. (C) Flow cytometry results of annexin V/PI staining of NPCs cultured with the supernatant. (D) Quantification of the apoptosis rate by the sum of the proportion of annexin V+ PI− and annexin V+ PI+ cells. (E) Western blot detection of the expression levels of catabolic proteins (MMP3 and MMP13) and anabolic proteins (COL2A1 and SOX9) in treated NPCs. (F) Densitometric analysis of matrix-related proteins in NPCs treated with supernatant. The fold change was normalized to the H_2O_2 (−)/MnO_2@TMNP (−) group. (G) Immunofluorescence staining of MMP3, MMP13, COL2A1, and SOX9 in treated NPCs. Scale bars: 50 μm. Data are presented as the mean ± SD (n = 3); ns, not significant; *, $p < 0.05$; **, $p < 0.01$; ***, $p < 0.001$; ****, $p < 0.0001$ between groups.

markers by LPS was not affected by MnO_2 nanoparticles but was significantly inhibited by TMNP and MnO_2@TMNP materials, which may be attributed to the binding and neutralization of LPS to the macrophage membranes. Furthermore, ELISA assays showed that the application of TMNP and MnO_2@TMNP reduced the content of TNF-α, IL-1β, IL-6, and IFN-γ in the supernatant of macrophages (Figure 5H−K). These results indicated that the neutralizing effects of macrophage membranes on LPS were effective in inhibiting M1 macrophage polarization and reducing proinflammatory cytokine accumulation.

MnO_2@TMNP Inhibits M1 Polarization by Removing ROS in Macrophages. The excessive production of ROS in macrophages during IDD needs to be cleared, as we discussed before. The nanomaterial coated with the macrophage cell membrane theoretically has a macrophage affinity, which may target macrophages.[36,37] This property of the macrophage cell membrane provides support for the specific clearance of ROS in

https://doi.org/10.1021/acsnano.3c08097
ACS Nano 2024, 18, 3053−3072

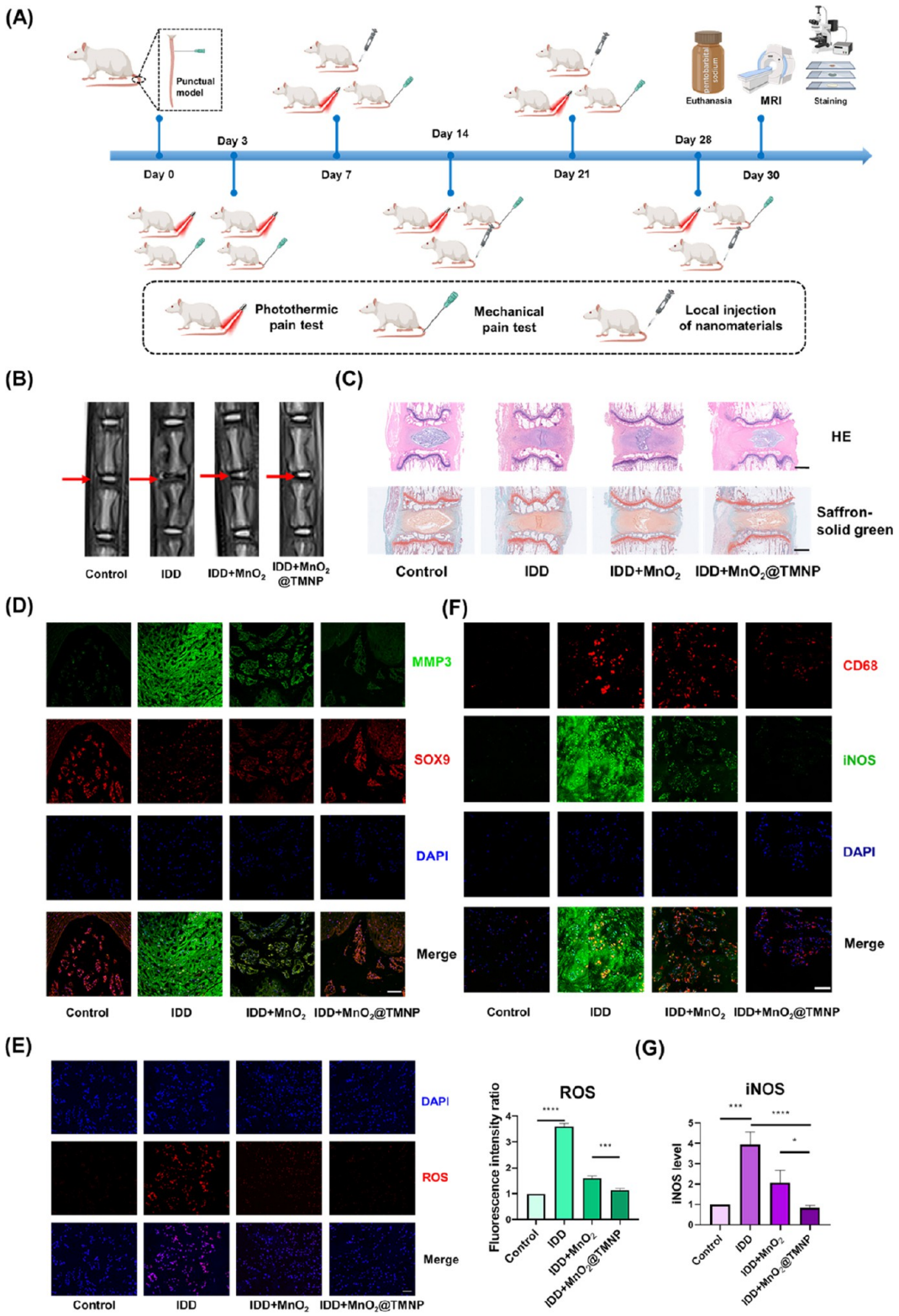

Figure 9. Protective effects of MnO_2@TMNP against disc degeneration by modulating the oxidative and inflammatory microenvironment. (A) Flowchart of the timing of in vivo experiments to evaluate the effects of MnO_2@TMNP on disc regeneration. (B) Representative T2-weighted MRI images of surgically punctured caudal vertebral discs of the control group, IDD group, IDD+MnO_2 group, and IDD+MnO_2@TMNP group. The red arrow marks the modeled section. (C) HE staining and Safranin O solid green staining of target segments of IVDs in different treatment groups. Scale bars: 1 mm. (D) Immunofluorescence staining of MMP3 and SOX9 in the surgically punctured IVD in different treatment groups. Scale bar: 100 μm. (E) Immunofluorescence staining and quantification of ROS in the surgically punctured IVD in different treatment groups. The fold change was normalized to control group. Scale bar: 50 μm. (F) Costaining of CD68 and iNOS to indicate the presence of M1-type macrophages in the surgically punctured IVD in different treatment groups. Scale bar: 100 μm. (G) The relative expression level of iNOS (normalized to control group). Data are presented as the mean ± SD (n = 3): ***, p < 0.001; ****, p < 0.0001 between groups.

https://doi.org/10.1021/acsnano.3c08097
ACS Nano 2024, 18, 3053−3072

macrophages. Therefore, we first evaluated the macrophage-specific affinity of MnO_2@TMNP nanoparticles. The main cells in the IVD microenvironment, NPCs, AFCs, CEPCs, and macrophages, were stained with different fluorescent dyes and then cocultured with nanomaterials loaded with DiO for 4 h for flow cytometry (Figure 6A). We found that the specific targeting of MnO_2@TMNP to macrophages was the most significant (Figure 6B,C). We loaded TMNP with DiO to obtain DiO-loaded MnO_2@TMNP and cocultured it with DiD-loaded macrophages. DiO-loaded MnO_2@TMNP fused with the membrane of macrophages, indicating a successful membrane integration (Figure 6D). We then cocultured MnO_2@TMNP loaded with red fluorescence ICG (the outer membrane was not loaded with fluorescent dye; ICG was loaded on the inner MnO_2) with macrophages overnight and found significant accumulation of MnO_2 in macrophages (Figure S3). Next, we studied the H_2O_2 removal capability of the nanoparticles and found that a small amount of H_2O_2 decomposed when added to TMNP, while MnO_2 nanoparticles and MnO_2@TMNP showed a high H_2O_2 decomposition capacity. The increase in dissolved oxygen content in the solution was confirmed by a dissolved oxygen measurement test (Figure 6E). After pretreating with H_2O_2, macrophages were cocultured with nanoparticles to evaluate their effects on scavenging intracellular ROS. We found that ROS in macrophages significantly increased after artificial addition of H_2O_2. TMNP alone did not effectively remove H_2O_2 in the cells, while MnO_2@TMNP nanoparticles showed noticeable H_2O_2 removal. MnO_2 nanoparticles without TMNP also decreased intracellular ROS, but the efficiency was significantly lower than that of MnO_2@TMNP (Figure 6F). This further indicated that MnO_2@TMNP had a higher efficiency for uptake by macrophages.

Then, we evaluated the effects of the nanoparticles on H_2O_2-induced M1 polarization (Figure 7A). We initially supplemented the medium with 5 μmol/L H_2O_2 and cultured the cells for 6 h, then changed the medium and added PBS or different nanomaterials (50 μg/mL) with a subsequent incubation for 24 h. We noticed that after coculture of H_2O_2 with M0 macrophages, the proportion of M1 macrophages significantly increased, while MnO_2 nanoparticles and MnO_2@TMNP downregulated M1 polarization (Figure 7B−D). MnO_2 nanoparticles were less effective in inhibiting H_2O_2-induced M1 polarization than was MnO_2@TMNP (Figure 7D), which may be related to the less efficient uptake of MnO_2 by macrophages. Similarly, the expression levels of M1-related markers in macrophages were elevated, and this upward trend was not suppressed by TMNP alone but was inhibited by MnO_2 nanoparticles and MnO_2@TMNP (Figure 7E−G). Uncoated MnO_2 nanoparticles exhibited a weaker inhibition effect than that of MnO_2@TMNP (Figure 7E−G). H_2O_2 increased the levels of TNF-α, IL-1β, IL-6, and IFN-γ in the medium, while MnO_2@TMNP downregulated the accumulation of inflammatory cytokines to a greater extent than did the MnO_2 nanoparticles (Figure 7H−K). TMNP also decreased the content of inflammatory cytokines in the medium, which was comparable to that of MnO_2@TMNP. We hypothesized that although TMNP nanoparticles alone had no clear anti-H_2O_2 effects, the binding of cytokines to TMNP could lead to their low levels of accumulation in the medium (Figure 7H−K). These results confirmed that MnO_2@TMNP nanoparticles were specifically taken up by macrophages with an intracellular release of MnO_2 that efficiently cleared the ROS to avoid the polarization of M1 macrophages and the formation of an inflammatory microenvironment.

MnO_2@TMNP Prevents IVD Cell Death and Regulates Extracellular Matrix Metabolism in an Inflammatory Microenvironment. A large number of proinflammatory cytokines, such as TNF-α and IL-1β produced by increasing M1-polarized macrophages, can induce apoptosis of NPCs, which is an important pathological cause of the progression of IDD.[9−12] We simulated the inflammatory microenvironment in IVDs by inducing M1 macrophage polarization with H_2O_2 and treated macrophages with or without MnO_2@TMNP. The supernatants were extracted to evaluate the effects of nanoparticles on NPC survival and matrix metabolism in an inflammatory microenvironment (Figure 8A). We found that NPC viability was significantly impaired when treated with the supernatants from H_2O_2-pretreated macrophages, which was reversed by MnO_2@TMNP (Figure 8B). Apoptosis analysis by flow cytometry further confirmed that the cell death rate was significantly upregulated in the H_2O_2 group, while MnO_2@TMNP treatment inhibited the proapoptotic effects of the inflammatory microenvironment (Figure 8C,D). The supernatants from H_2O_2-stimulated M1 macrophages clearly promoted the expression of catabolic proteins (MMP3 and MMP13) and downregulated the expression of anabolic proteins (COL2A1 and SOX9), indicating matrix degradation (Figure 8E,F). The application of MnO_2@TMNP significantly improved matrix deposition by increasing the expression of COL2A1 and SOX9 and decreasing the levels of MMP3 and MMP13 (Figure 8E,F). Immunofluorescence staining validated the findings in a Western blot analysis (Figure 8G and Figure S4). These findings demonstrated the beneficial impact of MnO_2@TMNP on cell survival and extracellular metabolic processes by mitigating M1 macrophage polarization induced by ROS. Although MnO_2@TMNP did not completely eliminate the effect of H_2O_2 on macrophages, the damage to NPCs by H_2O_2 influencing M1 macrophages was significantly reduced by MnO_2@TMNP.

MnO_2@TMNP Inhibits Disc Degeneration by Relieving the Local Inflammatory Microenvironment. We further evaluated the effects of MnO_2@TMNP on disc degeneration and pain behavior in the rat tail IDD model (Figure 9A). Local injection of nanoparticles was performed every 7 days from the seventh day after modeling, using a microinjector. The control group was injected with normal saline. MRI T2-weighted imaging was applied to evaluate the degenerative degree of the discs (Figure 9B). The intensity of the nucleus pulposus, indicating the hydration of tissues, was impaired in the IDD group compared to the control group, while MnO_2@TMNP significantly improved the intensity (Figure 9B). The modified Pfirrmann grading system based on MRI images was applied to evaluate the severity of IDD. MnO_2@TMNP decreased the relatively high degenerative grade in the IDD group. The recovery of disc degeneration from the MnO_2 nanoparticles was limited (Figure S5). Quantitation of the water content showed a significant loss of NP hydration in the IDD group, and the injection of MnO_2@TMNP improved NP hydration, while MnO_2 nanoparticles showed less-efficient hydration retention effects at the fourth week (Figure S5). HE staining and Safranin O solid green staining showed that in the IDD group, the structure of the IVD was severely disrupted, and the level of glycosaminoglycan was significantly decreased. Injection of MnO_2@TMNP effectively alleviated the progression of the lesion (Figure 9C). Immunofluorescence staining showed that

https://doi.org/10.1021/acsnano.3c08097
ACS Nano 2024, 18, 3053−3072

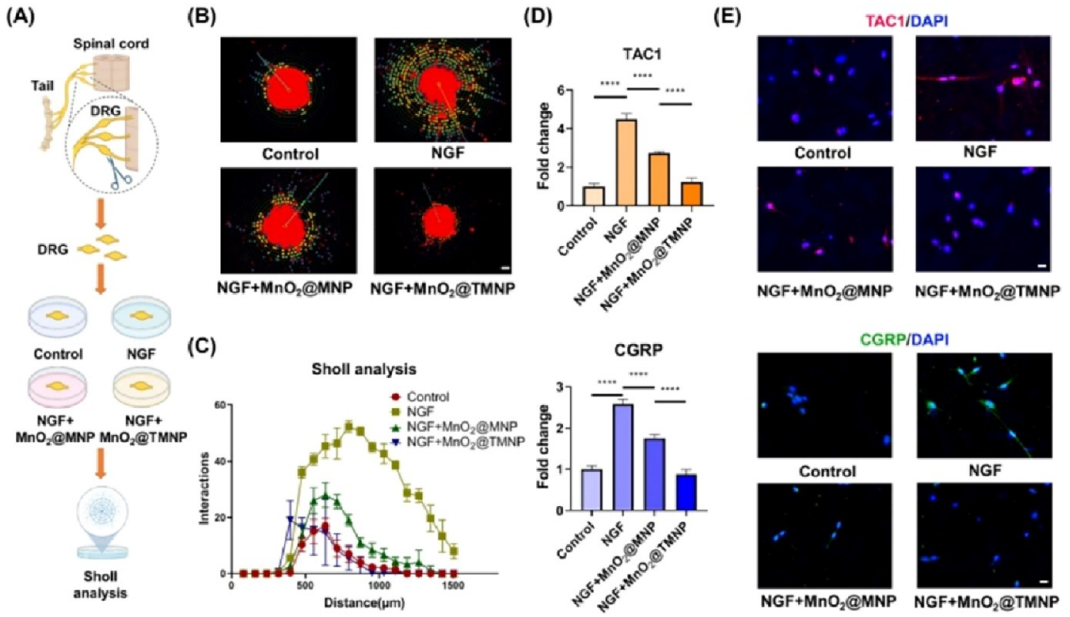

Figure 10. MnO_2@TMNP reduces sensory nerve growth and sensitization. (A) Schematic of the isolation, culture, and evaluation of DRGs. (B) Immunofluorescence staining of NF200 showing the axon growth pattern of DRGs cultured in NGF with or without nanoparticles. Scale bar: 200 μm. (C) Sholl analysis showing the effect of nanoparticles on NGF-promoted neurite growth in the ex vivo cultured DRG model. (D) The mRNA expression of TAC1 and CGRP of neurocytes treated with NGF, NGF+MnO_2@MNP, or NGF+MnO_2@TMNP. The fold change was normalized to the control group. (E) Immunofluorescence experiments showing the expression of TAC1 and CGRP in neurocytes after different treatments. Scale bars: 20 μm. Data are presented as the mean ± SD (n = 3): ****, p < 0.0001.

the expression level of SOX9 was restored, while MMP3 was suppressed in the MnO_2@TMNP group, indicating that MnO_2@TMNP effectively inhibited the disruption of stromal metabolism in the IDD model (Figure 9D and Figure S6). ROS staining of the entire IVD tissue showed that both MnO_2 nanoparticles and MnO_2@TMNP treatments demonstrated ROS clearance (Figure 9E). The MnO_2@TMNP nanoparticles were also observed to significantly reduce the iNOS expression level in CD68+ cells in the disc tissue, which indicated a downregulation of M1-type macrophages in the local microenvironment (Figure 9F). iNOS levels in intervertebral disc tissues were significantly reduced (Figure 9G). To summarize, the regenerative effects of MnO_2@TMNP were more clear than those of the MnO_2 nanoparticles, which may be attributed to better clearance of ROS in macrophages and modification of the inflammatory microenvironment.

MnO_2@TMNP Blocks the Growth of Sensory Nerves and Pain Sensitization. Pain is an important manifestation in the process of disc degeneration that imposes a heavy burden on quality of life.[5] The occurrence of pain in disc degeneration is highly correlated with nerve ingrowth into the inner part of the annulus fibrosus and nucleus pulposus.[38] MnO_2@TMNP nanoparticles contain abundant TrkA, which showed a satisfactory binding affinity to NGF (Figure 3F). We assessed the effects of MnO_2@TMNP nanoparticles on nerve growth and the production and release of pain transmitters. We collected DRGs and cultured them with NGF and nanoparticles in an ex vivo model (Figure 10A). Through immunofluorescence staining of NF200 and Sholl analysis that evaluates neurite branching and axon length distance from the cell body, we observed that MnO_2@TMNP effectively inhibited neurite extension induced by NGF (Figure 10B,C). Sensory neuropeptides in the pain pathway, including Tachykinin Precursor 1 (TAC1) and calcitonin gene-related peptide (CGRP), were positively associated with sensory sensitization in discogenic pain.[20,39] We found that MnO_2@TMNP reversed the increased levels of expression of TAC1 and CGRP induced by NGF in DRGCs (Figure 10D). Immunofluorescence staining also revealed that both MnO_2@MNP and MnO_2@TMNP decreased the expression of TAC1 and CGRP, while the inhibitory effects of MnO_2@TMNP were more noticeable (Figure 10E and Figure S7). These findings confirmed that MnO_2@TMNP alleviated the NGF-induced growth of sensory nerves and pain signaling activation.

MnO_2@TMNP Inhibits the Pain-Transmitting Pathway and Relieves Hyperalgesia to Inhibit Discogenic Pain. The pain behavior of rats was measured by the Von Frey mechanical threshold test (50% withdrawal threshold) and thermal threshold test (Hargreaves test).[40] We observed comparable pain thresholds among groups that had undergone disc puncture on the third day postmodeling, with a moderately decreased threshold with the sham group (in which only the skin was punctured) (Figure 11A,B). Then, rats were injected with normal saline, MnO_2, MnO_2@MNP, or MnO_2@MNP, and the painful behavior was recorded on days 7, 14, 21, and 28. The IDD group showed the most pronounced pain effects, as evidenced by its significantly lower thermal and mechanical pain thresholds compared to the sham group on day 28, indicating the successful establishment of the discogenic pain model. Injection of MnO_2 nanoparticles and MnO_2@MNP resulted in limited levels of pain inhibition, while injection of MnO_2@TMNP caused a significant analgesic effect with the threshold returning to the level of the sham group by day 28. Additionally, immunofluorescence staining was used to detect the levels of c-FOS (an index of neural activation) and GFAP (a marker of astrocyte activation) in the corresponding innervated segments of the spinal cord.[41,42] We found that injection of MnO_2@TMNP downregulated c-FOS and GFAP in spinal cord segments compared with the IDD group (Figure 11C,D and Figure S8). CGRP and TAC1 expression in the corresponding

https://doi.org/10.1021/acsnano.3c08097
ACS Nano 2024, 18, 3053−3072

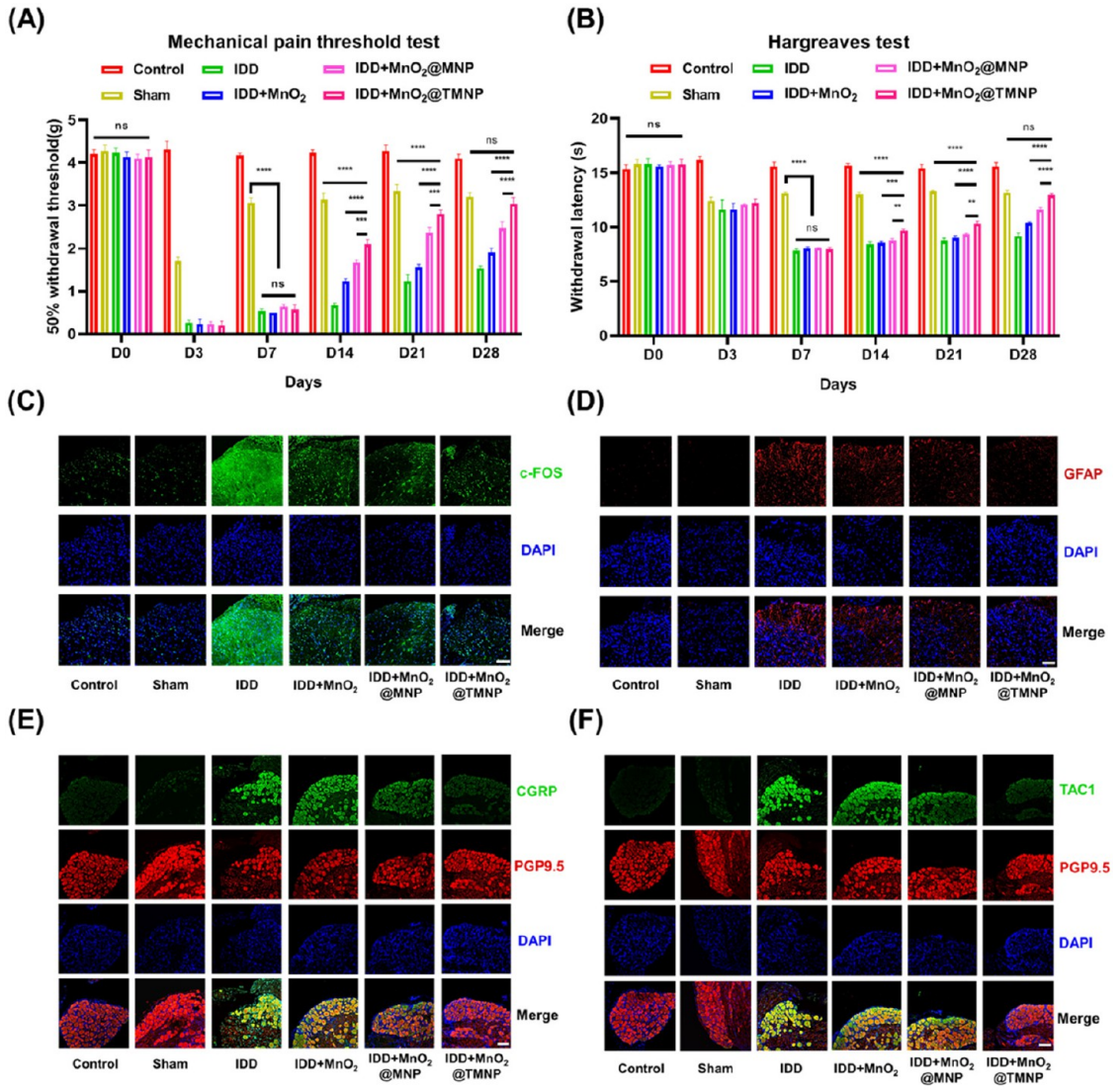

Figure 11. MnO_2@TMNP disrupts the pain signaling pathway and relieves discogenic pain. (A) 50% withdrawal thresholds detected by the von Frey test showing the mechanical threshold in the sham group, IDD group, IDD+MnO_2 group, IDD+MnO_2@MNP group, and IDD+MnO_2@TMNP group. (B) Hargreaves tests detecting painful behavior in response to heat stimulation of different groups. (C) c-FOS immunofluorescence staining of the spinal cord corresponding to caudal vertebral segments after different treatments. Scale bar: 50 μm. (D) GFAP immunofluorescence staining of the spinal cord corresponding to caudal vertebral segments. Scale bar: 50 μm. (E) CGRP immunofluorescence staining of DRGs innervating the coccygeal vertebrae. Scale bar: 100 μm. (F) TAC1 immunofluorescence staining of DRGs innervating the coccygeal vertebrae. Scale bar: 100 μm. Data are presented as the mean ± SD (n = 3): ns, not significant; **, p < 0.01; ***, p < 0.001; ****, p < 0.0001.

DRGs also showed significant upregulation in the IDD group, compared with the control group, and was downregulated most significantly in the MnO_2@TMNP group (Figure 11E,F and Figure S9). Moreover, MnO_2 nanoparticles and MnO_2@MNP also inhibited the expression of c-FOS and GFAP in the spinal cord, and the expression of TAC1 and CGRP in DRGs, but the effects were less apparent than those of MnO_2@TMNP. These results indicated that scavenging ROS and inflammatory cytokines is a feasible approach to inhibit hyperalgesia. Moreover, the overexpression of TrkA on the membrane endowed MnO_2@TMNP with a greater capacity for removing NGF, which may contribute to the increased pain inhibitory effects.

DISCUSSION

The inflammatory response in disc degeneration exacerbates the progression of degenerative changes.[43] The irregulated immune microenvironment during disc degeneration has been demonstrated by many studies.[44] The levels of various proinflammatory factors, including IL-1, IL-6, and TNF-α, are significantly elevated in degenerative IVDs.[45] In our study, we utilized MnO_2 nanoparticles coated with an engineered macrophage cell membrane overexpressing TrkA to tackle the aforementioned issues. We found that macrophage membrane showed high efficiency in removing various cytokines and LPS. The macrophage cell membrane exhibited expression of receptors for inflammatory factors/LPS, including IL-6R, IL-1R, TNFR, TLR4, and IFN-γR, which bound cytokines such as IL-6, IL-1, TNF-α, LPS, and IFN-γ, respectively.[30,46−48] These receptors serve as initiation switches for downstream proinflammatory

https://doi.org/10.1021/acsnano.3c08097
ACS Nano 2024, 18, 3053−3072

pathways, which trigger proinflammatory polarization. Interestingly, this process of the receptor−ligand reaction also provides conditions for efficiently decoying inflammatory factors. Previously, Shi et al. developed electroporation based membrane-coated nanoparticles for inflammatory factor absorption, demonstrating the feasibility of our design.[49]

An important activated manifestation of the inflammatory immune microenvironment is the polarization of macrophages toward the M1 phenotype.[50] Current research primarily focuses on the regulation of inflammatory-related signaling pathways, such as MAPK and NF-κB, to regulate M1 macrophage polarization.[51,52] The signaling pathways such as MAPK and NF-κB may be strongly associated with ROS.[53] The aforementioned pathways can induce macrophages to polarize toward the M1 phenotype, thereby resulting in the establishment of an inflammatory microenvironment. Disc degeneration is associated with adverse environments such as trauma and oxidative stress, in which ROS levels are often high.[54,55] Thus, ROS play a pivotal role in triggering the local immune microenvironment to initiate inflammation.[56] Following the activation of inflammation due to elevated levels of ROS, M1-type macrophages may generate additional increased ROS, thereby establishing a detrimental cycle that exacerbates the disease.[23] Therefore, efficient elimination of ROS is crucial in preventing the progression of the disc degenerative microenvironment toward inflammation. We selected MnO_2 nanoparticles as a ROS scavenger in this study due to their well-established antioxidant properties.[57] In our study, the in vitro antioxidant capacity of MnO_2 nanoparticles was confirmed by assessing their ability to decompose H_2O_2 with high efficiency. Therefore, MnO_2 nanoparticles can serve as a tool for ROS clearance to prevent macrophage polarization toward M1. In addition, the main target of our study is to clear intracellular and extracellular ROS, especially intracellular ROS. This is because the current mainstream view is that biogenic ROS are mainly produced in the mitochondria within the cell and are related to stress, starvation, and other factors.[58,59] The extracellular ROS may be related to the overflow of intracellular ROS after the destruction of cells. At present, there is some evidence that ROS mainly play an important role in cells instead of out of cells, including damaging DNA and regulating proteins or signaling pathways.[59−61] The regulation of ROS on macrophages is mainly intracellular.[62] Some studies on the regulation of ROS to control macrophage function have also focused on intracellular ROS levels.[63] These results confirm the necessity of regulating the ROS level in macrophages. So how to properly target MnO_2 nanoparticles into macrophages is important. In this study, we found that MnO_2@TMNP showed better effects on scavenging intracellular ROS than did MnO_2 nanoparticles, resulting in satisfactory M1 polarization inhibition. Targeting via the cell membrane is a highly efficient method due to the membrane homology, as well as the high efficiency of both membrane integration and ligand−receptor/molecule−molecule-mediated affinity.[27] Currently, homologous cell membrane targeting has been well documented, including the targeting of tumor cells or chondrocytes via tumor cell membranes or cartilage cell membranes.[36,64] Therefore, cell-membrane-mediated cellular uptake of the nanoparticles for MnO_2@TMNP may facilitate the intracellular ROS scavenging effects of MnO_2 nanoparticles. We believe that the use of TMNP in MnO_2@TMNP nanomaterials plays the following crucial roles in regulating macrophages. (A) TMNP imparts targeting capabilities to MnO_2, allowing MnO_2 to accumulate more effectively in macrophages for better ROS clearance. Our research confirmed that MnO_2@TMNP nanomaterials exhibited superior ROS-clearing effects in macrophages compared to MnO_2 nanomaterials. (B) TMNP also serves as an adsorbent for inflammatory factors, preventing local inflammatory storms. We also confirmed that MnO_2 nanomaterials cannot effectively prevent the LPS-induced M1 polarization of macrophages. These factors underscore the necessity of using MnO_2@TMNP when targeting macrophages, as MnO_2 nanomaterials cannot achieve the aforementioned effects.

As a type of pain occurring during disc degeneration, discogenic back pain is closely associated with sensory nerve ingrowth and an inflammatory microenvironment.[38,65] Inflammatory activation causes IVD cells and immune cells to produce a large quantity of proinflammatory factors and NGF.[66] The release of NGF can be augmented by proinflammatory cytokines, such as IL-1β, from IVD cells.[67,68] Studies have demonstrated that NGF stimulates the function of sensory nerves, significantly contributing to the development of low back pain.[69] In contrast to phospholipid membranes that can be artificially synthesized, such as liposome membranes, cell membranes are derived from living cells. This renders the engineering of cell membranes distinct from that of liposomes. Engineered modifications of liposomes typically involves physical or chemical reactions, and its efficacy and impact may be challenging to regulate.[70] When aiming to introduce a specific protein onto the surface of a cell membrane, particularly a membrane protein, high-expression cell membranes can be extracted from living cells overexpressing the corresponding gene.[71] When TrkA is overexpressed in macrophages, the corresponding cell membrane is endowed with the ability to bind the target protein, NGF. The ligand−receptor binding is a natural state, and its efficiency is theoretically superior to that of artificially designed targeted binding. Currently, the therapeutic concept of utilizing TrkA-overexpressing macrophage membranes to decoy inflammatory factors and NGF for alleviating the inflammatory microenvironment and pain associated with disc degeneration has not been investigated. We have confirmed that the overexpression of TrkA on macrophage cell membranes plays a significant role in the adsorption of NGF, which ultimately leads to inhibition of sensory nerve growth and sensation.

In this study, MnO_2@TMNP was demonstrated to effectively modulate the local inflammatory immune microenvironment of IVDs and alleviate discogenic back pain. We confirmed that MnO_2@TMNP inhibited the M1 polarization of macrophages, thereby suppressing the secretion of proinflammatory factors and exerting an anti-inflammatory effect. Furthermore, MnO_2@TMNP also exhibited direct adsorption and clearance of proinflammatory factors and LPS in the microenvironment, thereby mitigating the positive feedback loop of immune activation. It is worth noting that these two functions are closely related and interdependent. The advantage of MnO_2@TMNP lies in its relatively simple design, yet diverse functions, batch reproducibility and stability, excellent biocompatibility, and promising clinical application prospects. MnO_2@TMNP may have great potential in the treatment of advanced stages of disc degeneration for patients who experience significant pain that cannot be alleviated by traditional medication.

STUDY LIMITATIONS

However, it should be noted that our research still has some limitations. We carefully and systematically analyzed the limitations of our study in the following aspects. (1)

https://doi.org/10.1021/acsnano.3c08097
ACS Nano 2024, 18, 3053−3072

Experimental design can be further improved: in this study, we focused on how to regulate macrophages and the levels of cytokines in the extracellular matrix to control the progression of IDD and the pain. Apoptosis of nucleus pulposus cells induced by M1-polarized macrophages is a significant factor in IDD progression. However, there are still other causes of apoptosis in nucleus pulposus cells. In this study, the nanomaterials we designed did not directly target nucleus pulposus cells. In future research, designing nanomaterials with more targeted functions (such as dual targeting of macrophages and nucleus pulposus cells through hybrid membrane-coated nanoparticles) to simultaneously achieve adsorption of inflammatory factors, suppression of macrophage M1-polarization, and protection of nucleus pulposus cells may be viable directions for further investigation. (2) The in vivo metabolism of nanomaterials remains unclear: in our study, we extensively demonstrated the biocompatibility of nanomaterials through both in vitro and in vivo experiments. However, the metabolic pathways of nanoparticles in vivo cannot be fully elucidated due to technological limitations. In the future, with the development of high-precision in vivo elemental tracing techniques, this issue may be further clarified. (3) Shortcomings in the administration of nanomaterials: the nanomaterials we designed were administered through a local injection. It is important to recognize that this method of administration carries a potential risk of further damage to the intervertebral disc and the exacerbation of pain. Therefore, in the future, enhancing the clinical application value can be achieved by further improving our nanomaterials and administering them in a noninvasive manner. (4) High storage requirements for nanomaterials: due to the inclusion of bioactive components in the MnO_2@TMNP nanomaterials, prolonged storage or inappropriate storage temperatures may result in the ineffectiveness of the nanomaterials. (5) Ethical and biosafety concerns: in the future, the cell membrane components used in clinical nanomaterials usually originate from human cells, which could raise ethical and biosafety concerns. The source and preparation process of the membrane must be strictly monitored.

CONCLUSION

MnO_2@TMNP nanomaterials have been proposed to modulate the inflammatory immune microenvironment in IVD and alleviate discogenic back pain. MnO_2@TMNP exhibited the ability to clear ROS in macrophages and extensively decoy inflammatory factors and NGF to prevent disc degeneration and pain transmission. The nanomaterial exhibited favorable biosafety, can be manufactured in large quantities, and possesses significant clinical applicability.

METHODS

Materials. 3,3′-dioctadecyloxacarbocyanine perchlorate (DiO), 1,1'-dioctadecyl-3,3,3',3'-tetramethylindocarbocyanine perchlorate (DiI), 1,1'-Dioctadecyl-3,3,3',3'-Tetramethylindodicarbocyanine,4-Chlorobenzenesulfonate Salt(DiD), ROS flow kit, and Western blot reagents were purchased from Beyotime Biotechnology (China). The cytokines used in this study (TNF-α, IL-1β, IL-6, interferon-γ (IFN-γ)), lipopolysaccharide (LPS), and NGF were purchased from MedChemExpress (MCE, China). Indocyanine green (ICG) was obtained from Macklin Inc. (China). The apoptosis flow kit and cell counting kit-8 (CCK-8) cell viability assay kit were purchased from Vazyme Biotech Co., Ltd. (China). The J774A.1 cell line was purchased from Procell Life Science & Technology Co., Ltd. (China). Lipofectamine 3000, PBS, media, serum, and ELISA kits required for cell culture were purchased from Thermo Fisher Scientific Inc. (Waltham, MA, USA). The PCR-related reagents were purchased from Yeasen Biotechnology Co., Ltd. (China). The animals needed for the experiment were purchased from the Laboratory Animal Center of Huazhong University of Science and Technology.

Generation of TrkA-Overexpressing Macrophage Cell Membranes. The J774A.1 murine monocyte macrophage cell line was cultured in a stable extracellular environment. Plasmids carrying the TrkA-encoding gene (*NTRK1*), FLAG tag, and GFP were delivered into J774A.1 cells using the Lipofectamine 3000 reagent. After the transfection procedure as instructed, cells were examined for GFP expression under a fluorescence microscope, and TrkA overexpression was confirmed via PCR experiments and Western blot assays. Subsequently, TrkA-overexpressing macrophages were washed with PBS and resuspended in the presence of protease inhibitors. Then, referring to a previous study,[72] TrkA-overexpressing macrophage membrane (TMNP) was obtained through differential centrifugation after repeated freezing and thawing using liquid nitrogen, before being stored at −80 °C for future use. In addition, macrophages without TrkA overexpression were prepared to extract MNP according to the same protocol.

Synthesis of Nanomaterials. The permanganate reduction method was utilized for the synthesis of MnO_2 nanoparticles.[73,74] Polymorphic MnO_2 particles with diameters of about 400−500 nm were obtained by particle size screening. The nanoparticles obtained were subjected to ultrapure water washing followed by drying and storage. The cell membrane coating was generated using an extruder (Genizer HandExtruder-1 mL, USA). We initially passed the extracted macrophage membranes through an extruder equipped with polycarbonate porous membranes of 1 μm and 800 nm pore sizes, respectively, to obtain vesicles of relatively uniform size. The vesicles were mixed with MnO_2 nanomaterials in a 1:1 mass ratio and then passed through a 600 nm pore size polycarbonate membrane to obtain membrane-encapsulated nanoparticles. The encapsulation process was consistent whether using the membrane of macrophages overexpressing TrkA or control plasmids. Each extrusion process was repeated at least 50 times.

Physicochemical Characterization. The structure of the synthesized MnO_2 nanomaterials was first observed by scanning electron microscopy (SEM) (ZEISS GeminiSEM 300) and transmission electron microscopy (TEM) (FEI Talos F200X). The composition of the nanomaterials was confirmed by energy spectrum tests. The morphology of membrane vesicles and membrane-coated nanomaterials were observed by low-voltage TEM (Hitachi HT7800). A negative dyeing technique was employed, utilizing 1% phosphotungstic acid as the negative dyeing reagent for a duration of 30 s. The nanomaterial hydrated particle size and zeta potential were determined using a Malvern Zetasizer Nano ZS90 instrument. During the zeta potential measurement, the pH was adjusted to 7.4.

Oxygen Determination. We monitored bubble formation to ascertain the production of O_2, and we utilized a portable dissolved oxygen meter (REX, JPSJ-605F, China) to quantify the oxygen concentration. One percent H_2O_2 was used in vitro and incubated with PBS, 50 μg/mL MNP, 50 μg/mL TMNP, 50 μg/mL MnO_2, 50 μg/mL MnO_2@MNP, or 50 μg/mL MnO_2@TMNP. The reaction was conducted in a 1.5 mL Eppendorf (EP) tube to observe the formation of bubbles. Similarly, the reaction was carried out under identical conditions in a beaker while measuring dissolved oxygen levels every minute and plotting the corresponding curve. Distilled water served as the baseline for dissolved oxygen measurements under equivalent conditions.

Cell Extraction and Culture. In this study, nucleus pulposus cells (NPC), annulus fibrosus cells (AFC), cartilage end plate cells (CEPC), and ganglion cells were extracted from rats. The extraction steps for NPC and AFC were as described in previous studies.[75,76] CEPC and dorsal root ganglion cells (DRGC) were obtained by continuous enzymatic digestion. After the rat was anesthetized, sterilized, and covered in a routine manner, the spine was surgically exposed and the cartilage end plate tissue was meticulously dissected. The blood was carefully rinsed off with Hank's balanced salt solution. The tissue blocks were then cut to <1 mm^3 on a sterile benchtop and digested with 0.2%

https://doi.org/10.1021/acsnano.3c08097
ACS Nano 2024, 18, 3053−3072

collagenase (type I/II as needed) at 37 °C . The mixture was centrifuged at 1200 rpm for 3 min, and the supernatant was discarded. Then, 0.25% trypsin was added for digestion at 37 °C The mixture was centrifuged at 1200 rpm for 3 min. Finally, complete medium was added and centrifuged three times. The cells were resuspended with an appropriate medium and cultured in a cell incubator. NPC, AFC, and CEPC were treated with medium containing DMEM/F12 medium with 10% fetal bovine serum and 1% penicillin/streptomycin. Macrophages (J774A.1 cell line) were treated with DMEM with 4.5 g/L glucose, 10% fetal bovine serum, and 1% penicillin/streptomycin. DRGC were treated with medium containing Neurobasal-A, IB-27 supplement, 1% penicillin/streptomycin, and GlutaMAX supplement (Procell Life Science & Technology Co., Ltd., China). The cell culture environment was 37 °C and 5% CO_2.

Sholl Analysis. After the ganglion immunofluorescence plots were obtained, an analysis was performed using Sholl analysis (4.2.0) in ImageJ 1.54 software. Once the threshold of the plot was set correctly to clear the background, analysis was performed. The set radius step was 79.167 μm, and the number of intersection points was calculated automatically by the software and displayed in the form of a line chart.

CCK-8 Test. In this study, the CCK-8 assay was used to determine the cell viability. The cells were seeded uniformly onto 96-well plates at a density of 5000 cells per well. The experimental treatment was subsequently conducted, and then, the initial medium was removed. The CCK-8 working solution was prepared using serum-free medium and coincubated with the cells at 37 °C for 2 h, protected from light. Following incubation, the absorbance at 450 nm was quantified by using an enzymatic marker. Additionally, a blank control group consisting of a CCK-8 working solution not incubated with cells was utilized. When the results were interpreted, the background absorbance from the blank control group was subtracted.

Polymerase Chain Reaction (PCR). After cell treatment, the RNA was extracted on a sterile operating table. The extraction process was carried out under ice-cold conditions. RNA isolation was performed by using a FastPure Cell/Tissue Total RNA Isolation kit V2 (Vazyme Biotech Co., Ltd.). The concentration of purified RNA was determined with a NanoDrop spectrophotometer. The cDNA was synthesized through reverse transcription, with a reaction temperature of 55 °C and a duration of 30 min. The reverse transcriptase was subsequently inactivated at 85 °C for 5 min to prepare for PCR. The condition of predenaturation was 98 °C for 2 min. Following the instructions, denaturation was carried out at 98 °C for 30 s, followed by annealing at 60 °C for 30 s. The final extension step was performed at 72 °C for a duration of 1 min. The number of annealing/extension cycles was set to 50. The cycle threshold (CT) was acquired using a fluorescent quantitative real-time PCR instrument (Bio-Rad CFX96). The fold changes were calculated following the 2-$\Delta\Delta CT$ method with GAPDH levels for normalization. Primer information is shown in Table S1.

Apoptosis Flow Cytometry and ROS Detection. In this study, the level of apoptosis in cells was assessed by using flow cytometry. Following cell treatment, apoptotic cells were initially collected from the supernatant and subsequently dissolved in PBS for analysis. PBS was used to clean the adherent cells, and EDTA-free trypsin was used for digestion. Then, the cells were resuspended in PBS and mixed with the corresponding apoptotic cells that had been previously collected. Cells were centrifuged at 3000 rpm for 3 min to collect the precipitate. Subsequently, the suspended cells were washed twice with precooled PBS. After precipitation of cells, 100 μL of 1 × binding buffer was added and annexin V-FITC and propidium iodide (PI) staining were performed separately. The dyeing process was conducted under ambient temperature in a light-free environment. Following staining, 400 μL of 1 × binding buffer was added, and then the cells were analyzed using flow cytometry (Accuri C6 Plus, BD, New Jersey, USA). Intracellular ROS levels were observed by ROS flow cytometry. 2′,7′-Dichlorodihydrofluorescein diacetate (DCFH-DA) was diluted in serum-free medium at a ratio of 1:3000. The staining solution was then added to the cells and incubated in a cell incubator at 37 °C for 20 min. Cells were manually inverted and mixed every 5 min. Following the reaction, cells were washed three times with serum-free medium and then collected and analyzed using flow cytometry (Accuri C6 Plus, BD).

Polarization Analysis of Macrophages by Flow Cytometry. In this study, fluorescent antibodies were utilized to label F4/80, CD11b, CD86, and CD206 (BioLegend, Inc., US; CAS 123131, 101205, 159204, and 141716) on the surface of macrophages. The polarization state of macrophages was determined by analyzing the levels of these proteins by flow cytometry. Antibodies targeting CD32 (BioLegend, Inc., US; CAS 156402) were subsequently introduced to obstruct the Fc receptor on the macrophage surface. The cells were thoroughly washed and incubated with anti-CD11b, anti-F4/80, and anti-CD86 at ambient temperature for 30 min. The suspended cells were subsequently washed, and the macrophages were permeabilized and immobilized using a membrane-disrupting/immobilizing solution. The macrophages were labeled and stained with anti-CD206, followed by a subsequent washing step prior to detection using flow cytometry (Accuri C6 Plus, BD).

Membrane Fusion and Uptake of Nanomaterials. The specific interaction between macrophages and nanomaterials was quantified by flow cytometry, while membrane fusion and uptake of the nanomaterials were visualized by using confocal microscopy. To determine the precise affinity between macrophage energy and nanomaterials, we initially labeled the cell membranes of NPC, AFC, CEPC, and macrophages using various combinations of DiI, DiD, and Hoechst 33342. The specific grouping methodology is outlined in Results. The cells were digested, resuspended, mixed, and cocultured. Once the cells had adhered stably to the plate, DiO-supported nanomaterials were introduced at a concentration of 50 μg/mL for coculture with the cells. Following an overnight culture, the supernatant was discarded and the cells were subsequently washed with PBS, before being detected by flow cytometry. FlowJo v10.4 was utilized to analyze the uptake of nanomaterials by cells. The uptake of the nanomaterials by macrophages was observed by confocal microscopy. Nanomaterials loaded with ICG (ICG was adsorbed by MnO_2 and the macrophage membrane was not loaded with fluorescent dye) were added at a dose of 50 μg/mL. Following an overnight culture for 8 h, the supernatant was discarded and the cells were thoroughly washed with PBS. The phagocytic activity of the materials was subsequently visualized using confocal microscopy (Olympus, Japan) after staining with phalloidin and DAPI. Moreover, the MnO_2 nanoparticles were coated with the DiD-loaded cell membrane, while MnO_2 itself was not loaded with fluorescent dye. DiO-stained macrophages were cultured with DiD-loaded nanomaterials at a concentration of 50 μg/mL for 8 h. Then, after staining with DAPI, the cells were washed with PBS and visualized by confocal microscopy (Olympus, Japan).

Western Blot. The protein expression level was determined by using a Western blot assay. Membrane or total proteins were extracted and denatured with the Radio Immunoprecipitation Assay (RIPA) lysate. Protein transfer was performed following electrophoresis. Blocking occurred subsequent to transmembrane insertion. 5% Bovine Serum Albumin (BSA) was applied, and membranes were incubated at room temperature for 1 h. After blocking, the membranes were washed with Tris Buffered Saline with Tween 20 (TBST). Following the TBST washing, the membranes were separately incubated with primary and secondary antibodies at room temperature for a duration of 2 h. Subsequently, TBST was used for further cleaning prior to exposure to the chemiluminescence instrument (Bio-Rad ChemiDoc MP Imaging System, US). The antibody information used in this experiment is shown in Table S2.

Protein Distribution of Nanomaterials. We detected the protein distribution of nanomaterials by SDS-PAGE and Coomassie bright blue staining (kit purchased from Beyotime Biotechnology (China)). After the correct synthesis of the nanomaterials, the total protein of the nanomaterials was extracted. Then we proceeded to use SDS-PAGE. A protein ladder was used to confirm protein separation. Once the proteins had been successfully separated, we carefully removed the intact gel. We placed the gel in adequate Coomassie bright blue dye, which should cover the gel. The samples were then placed in a shaker and dyed at room temperature for 3 h. The dye was then removed, and a sufficient amount of decolorizing solution was added. The sample was then placed in a shaker and decolorized at room temperature, until the blue background was cleaned. The decoloring solution was changed 2−

https://doi.org/10.1021/acsnano.3c08097
ACS Nano 2024, 18, 3053−3072

3 times according to the instructions. Photographs were taken after the decolorization was complete.

Levels of Inflammatory Cytokines in Vitro and in Vivo. The levels of IL-1β, IL-6, TNF-α, IFN-γ, NGF, and LPS were quantified using an enzyme-linked immunosorbent assay (ELISA) (IL-1β, IL-6, TNF-α, IFN-γ, and NGF, Thermo Fisher Scientific Inc., Waltham, MA, USA; LPS, Shanghai Rayzbio Technology Co., Ltd., China). Adequate blank and negative controls were incorporated to ensure the precision of the outcomes. Different concentrations of standard products were added to the standard orifices with the correct volume. The samples were reconstituted by diluting and pipetting the sample into the designated wells but not the blank wells. The antibodies corresponding to the cytokines reacted with the standard and sample wells through incubation as indicated in the instructions. The reaction wells were sealed with a film and incubated at room temperature for 60 min. The plates were washed five times after the reaction. Then, the substrate was added to each well and incubated at room temperature in the dark for 15 min. Finally, the reaction was terminated, and the absorbance was measured.

Hemolytic Test. Red blood cells from SD rats were utilized for the hemolysis assay. The rats were properly immobilized under anesthesia, and the fur in the precardiac region was meticulously removed. Using fingertips, the most prominent pulsations were identified and marked. After iodophor disinfection, the site was punctured with a No. 5 needle attached to a syringe. Once the blood was automatically drawn into the syringe, 1 mL of the sample was extracted into a collection vessel containing heparin, which was gently and sufficiently shaken to prevent clotting. The red blood cells were isolated and suspended in PBS buffer at 3000 rpm for 3 min. The red blood cells in the PBS solution were cocultured with varying concentrations of nanomaterials at 37 °C for 3 h. A positive control group was established, wherein the red blood cells were placed in pure water. Following coculturing, the mixture was centrifuged at 12000 rpm for 10 min and the color of the supernatant was observed. The supernatant was then removed, and absorbance was measured at 541 nm before statistical analysis.

Immunofluorescent Staining. Immunofluorescent staining was employed to evaluate the intracellular protein expression level. The cells were counted and seeded onto slides, followed by treatment as required by the experiment. Subsequently, the medium was removed, and the cells were washed with PBS. Then, 4% paraformaldehyde was added for fixation. After fixation, the cells were incubated in a PBS solution containing 0.5% Triton for 15 min for permeation. After being washed with PBS, the cells were blocked with goat serum. The blocking process was carried out at 37 °C for 45 min, followed by washing with PBST. Subsequently, primary and secondary antibodies were incubated with the cells separately at room temperature for 2 h. After the incubation period, cells were washed with PBST. An antiquenching agent was added before reversing the cells on the slide for observation. The antibody information required in this experiment is shown in Table S3.

Animal Experiments. All animal experiments conducted in this study were approved by the university's ethics committee. The animal model employed in this investigation was the Sprague−Dawley (SD) rat. The animals were randomly divided into the following groups: control group, sham group, IDD group, IDD+MnO_2 nanoparticle group, IDD+MnO_2@MNP group, and IDD+MnO_2@TMNP group. The IDD model was established via coccygeal vertebra puncture, as previously described.[77] The control group received no puncture. The sham group was punctured by the same needle used in the IDD group, but only the corresponding area of the skin was punctured, leaving the discs intact. After modeling, the corresponding anatomical locations were marked and observed every 3 days. Treatment was initiated on the seventh day following modeling, with administration of medication or PBS (control group) into rat nucleus pulposus via a 29-G needle (Hamilton injection needle) with a dosage of 3 mg/kg unless otherwise specified. The injections were administered on a weekly basis with mechanical and thermal pain thresholds assessed prior to each injection. On the 30th day, the animals were euthanized for postobservation procedures. The spinal cord, ganglion, and IVD tissues were promptly extracted for subsequent PCR analysis, Hematoxylin-Eosin (HE) staining, safranin O fast green staining, and immunofluorescence labeling. In vivo organ toxicity detection was observed by injecting 3 mg/kg nanomaterials into blood vessels through the tail vein and collecting the major organs (heart, liver, spleen, lung, and kidney) for HE staining after 3, 14, and 30 days. Pain tests in animals were mainly performed using a mechanical pain threshold test and a Hargreaves test. The mechanical pain threshold was tested by using a Von Frey haptometer. We set 2 g as the initial test force, with adequate time intervals between different testing forces to allow the animals to fully recover their original state. Force was recorded when the animal had a significant pain response. The pain responses mainly included licking, flinching, withdrawing the tail, or squeaking. Tests were repeated three times for each animal. The results of this experiment were presented at the 50% withdrawal threshold. The filament weight and percentage response of each animal were recorded and tabulated. The 50% response versus time (days) was calculated from the above data. The average value of each group was calculated and plotted as a histogram. A rat tail light thermal pain meter (ZL-031, Anhui Yaokun Biotechnology Co., Ltd., China) was used to perform the Hargreaves test. We observed the time from the onset of heating to the appearance of significant pain in the rat's tail.

Statistics. GraphPad Prism 8 was used as comprehensive statistical analysis software. Unless otherwise specified, the differences between groups were analyzed using ANOVA (more than two groups) or *t*-tests (two groups). Data were presented as the mean ± standard deviation (SD), and statistical significance was set at $p < 0.05$.

ASSOCIATED CONTENT

Supporting Information

The Supporting Information is available free of charge at https://pubs.acs.org/doi/10.1021/acsnano.3c08097.

PCR primer information, Western blot antibody information, immunofluorescent antibody information, evidence of high expression of TrkA in macrophage cell membranes, protein distribution of different materials, uptake of MnO_2@TMNP into macrophages, statistical results of immunofluorescence of MMP3, MMP13, COL2A1, and SOX9 in treated nucleus pulposus cells, statistics of the Pfirrmann score and water content of treated IVDs analyzed by MRI (the ratio was normalized to the control group), statistical analysis of immunofluorescence staining of MMP3 and SOX9 in treated IVD tissue, statistics of the immunofluorescence staining results of TAC1 and CGRP in treated neurocytes, and immunofluorescence statistics of c-FOS and GFAP in the spinal cord innervating the coccygeal vertebra in different treatment groups (PDF)

AUTHOR INFORMATION

Corresponding Authors

Yizhong Peng − *Department of Orthopaedics, Union Hospital, Tongji Medical College, Huazhong University of Science and Technology, Wuhan 430022, People's Republic of China*; orcid.org/0000-0002-3646-3360; Email: pyz5941z@163.com

Xiangcheng Qing − *Department of Orthopaedics, Union Hospital, Tongji Medical College, Huazhong University of Science and Technology, Wuhan 430022, People's Republic of China*; Email: qingxc2016@hust.edu.cn

Zengwu Shao − *Department of Orthopaedics, Union Hospital, Tongji Medical College, Huazhong University of Science and Technology, Wuhan 430022, People's Republic of China*; Email: szwpro@163.com

https://doi.org/10.1021/acsnano.3c08097
ACS Nano 2024, 18, 3053−3072

Authors

Wenbo Yang − *Department of Orthopaedics, Union Hospital, Tongji Medical College, Huazhong University of Science and Technology, Wuhan 430022, People's Republic of China*

Kanglu Li − *Department of Orthopaedics, Union Hospital, Tongji Medical College, Huazhong University of Science and Technology, Wuhan 430022, People's Republic of China*

Qing Pan − *Department of Orthopaedics, Union Hospital, Tongji Medical College, Huazhong University of Science and Technology, Wuhan 430022, People's Republic of China*

Wei Huang − *Department of Orthopaedics, Union Hospital, Tongji Medical College, Huazhong University of Science and Technology, Wuhan 430022, People's Republic of China*

Yan Xiao − *Department of Radiology, Union Hospital, Tongji Medical College, Huazhong University of Science and Technology, Wuhan 430022, People's Republic of China*

Hui Lin − *Department of Orthopaedics, Union Hospital, Tongji Medical College, Huazhong University of Science and Technology, Wuhan 430022, People's Republic of China*

Sheng Liu − *Department of Orthopaedics, Union Hospital, Tongji Medical College, Huazhong University of Science and Technology, Wuhan 430022, People's Republic of China*

Xuanzuo Chen − *Department of Orthopaedics, Union Hospital, Tongji Medical College, Huazhong University of Science and Technology, Wuhan 430022, People's Republic of China*

Xiao Lv − *Department of Orthopaedics, Union Hospital, Tongji Medical College, Huazhong University of Science and Technology, Wuhan 430022, People's Republic of China*

Shiqing Feng − *The Second Hospital of Shandong University, Cheeloo College of Medicine, Shandong University, Jinan, Shandong 250033, People's Republic of China; Department of Orthopaedics, Tianjin Medical University General Hospital, Tianjin Medical University, International Science and Technology Cooperation Base of Spinal Cord Injury, Tianjin Key Laboratory of Spine and Spinal Cord, Tianjin 300052, People's Republic of China; Department of Orthopaedics, Qilu Hospital of Shandong University, Shandong University Centre for Orthopaedics, Advanced Medical Research Institute, Cheeloo College of Medicine, Shandong University, Jinan, Shandong 250012, People's Republic of China*

Complete contact information is available at: https://pubs.acs.org/10.1021/acsnano.3c08097

Author Contributions

W.Y., K.L., and Q.P. were responsible for the design of the experiment, data collection, and manuscript writing. W.H., H.L., Y.X., S.L., X.C., X.L., S.F., and X.Q. were responsible for the implementation of experiments, data collection, and figure plotting. X.Q., W.H., Z.S., and Y.P. were responsible for the review of manuscripts and financial support.

Author Contributions

#W.Y., K.L., and Q.P. share the first authorship.

Notes

The authors declare no competing financial interest.

ACKNOWLEDGMENTS

This work was supported by the National Natural Science Foundation of China (82202764, 82202763, 81974352, 82202765, 82002318, 82102627), China Postdoctoral Science Foundation (2021M701331), Wuhan Knowledge Innovation Project (2022020801020468), and Scientific Research Training Program for Young Talents from Union Hospital, Tongji Medical College, Huazhong University of Science and Technology. We thank LetPub (www.letpub.com) for its linguistic assistance during the preparation of this manuscript.

REFERENCES

(1) Sinkemani, A.; Wang, F.; Xie, Z.; Chen, L.; Zhang, C.; Wu, X. Nucleus Pulposus Cell Conditioned Medium Promotes Mesenchymal Stem Cell Differentiation into Nucleus Pulposus-Like Cells under Hypoxic Conditions. *Stem cells international* **2020**, *2020*, 8882549.

(2) Pan, H.; Strickland, A.; Madhu, V.; Johnson, Z. I.; Chand, S. N.; Brody, J. R.; Fertala, A.; Zheng, Z.; Shapiro, I. M.; Risbud, M. V. RNA binding protein HuR regulates extracellular matrix gene expression and pH homeostasis independent of controlling HIF-1α signaling in nucleus pulposus cells. *Matrix biology: journal of the International Society for Matrix Biology* **2019**, *77*, 23−40.

(3) Bento, T. P. F.; Genebra, C.; Maciel, N. M.; Cornelio, G. P.; Simeão, S.; Vitta, A. Low back pain and some associated factors: is there any difference between genders? *Brazilian journal of physical therapy* **2020**, *24*, 79−87.

(4) Casser, H. R.; Seddigh, S.; Rauschmann, M. Acute Lumbar Back Pain. *Deutsches Arzteblatt international* **2016**, *113*, 223−34.

(5) Mohd Isa, I. L.; Teoh, S. L.; Mohd Nor, N. H.; Mokhtar, S. A. Discogenic Low Back Pain: Anatomy, Pathophysiology and Treatments of Intervertebral Disc Degeneration. *International journal of molecular sciences* **2023**, *24*, 208.

(6) Fujii, K.; Yamazaki, M.; Kang, J. D.; Risbud, M. V.; Cho, S. K.; Qureshi, S. A.; Hecht, A. C.; Iatridis, J. C. Discogenic Back Pain: Literature Review of Definition, Diagnosis, and Treatment. *JBMR plus* **2019**, *3*, No. e10180.

(7) Kang, L.; Zhang, H.; Jia, C.; Zhang, R.; Shen, C. Targeting Oxidative Stress and Inflammation in Intervertebral Disc Degeneration: Therapeutic Perspectives of Phytochemicals. *Frontiers in pharmacology* **2022**, *13*, 956355.

(8) Wang, L.; He, T.; Liu, J.; Tai, J.; Wang, B.; Zhang, L.; Quan, Z. Revealing the Immune Infiltration Landscape and Identifying Diagnostic Biomarkers for Lumbar Disc Herniation. *Frontiers in immunology* **2021**, *12*, 666355.

(9) Ling, Z.; Liu, Y.; Wang, Z.; Zhang, Z.; Chen, B.; Yang, J.; Zeng, B.; Gao, Y.; Jiang, C.; Huang, Y.; Zou, X.; Wang, X.; Wei, F. Single-Cell RNA-Seq Analysis Reveals Macrophage Involved in the Progression of Human Intervertebral Disc Degeneration. *Frontiers in cell and developmental biology* **2022**, *9*, 833420.

(10) Zhao, F.; Guo, Z.; Hou, F.; Fan, W.; Wu, B.; Qian, Z. Magnoflorine Alleviates "M1" Polarized Macrophage-Induced Intervertebral Disc Degeneration Through Repressing the HMGB1/Myd88/NF-κB Pathway and NLRP3 Inflammasome. *Frontiers in pharmacology* **2021**, *12*, 701087.

(11) Li, X. C.; Luo, S. J.; Fan, W.; Zhou, T. L.; Tan, D. Q.; Tan, R. X.; Xian, Q. Z.; Li, J.; Huang, C. M.; Wang, M. S. Macrophage polarization regulates intervertebral disc degeneration by modulating cell proliferation, inflammation mediator secretion, and extracellular matrix metabolism. *Frontiers in immunology* **2022**, *13*, 922173.

(12) Zhang, S.; Wang, P.; Hu, B.; Liu, W.; Lv, X.; Chen, S.; Shao, Z. HSP90 Inhibitor 17-AAG Attenuates Nucleus Pulposus Inflammation and Catabolism Induced by M1-Polarized Macrophages. *Frontiers in cell and developmental biology* **2022**, *9*, 796974.

(13) Navone, S. E.; Marfia, G.; Giannoni, A.; Beretta, M.; Guarnaccia, L.; Gualtierotti, R.; Nicoli, D.; Rampini, P.; Campanella, R. Inflammatory mediators and signalling pathways controlling intervertebral disc degeneration. *Histology and histopathology* **2017**, *32*, 523−542.

(14) Yunna, C.; Mengru, H.; Lei, W.; Weidong, C. Macrophage M1/M2 polarization. *European journal of pharmacology* **2020**, *877*, 173090.

(15) Zhang, S.; Hu, B.; Liu, W.; Wang, P.; Lv, X.; Chen, S.; Shao, Z. The role of structure and function changes of sensory nervous system in intervertebral disc-related low back pain. *Osteoarthritis and cartilage* **2021**, *29*, 17−27.

(16) Pinho-Ribeiro, F. A.; Verri, W. A., Jr; Chiu, I. M. Nociceptor Sensory Neuron-Immune Interactions in Pain and Inflammation. *Trends in immunology* **2017**, *38*, 5−19.
(17) Aoki, Y.; Takahashi, Y.; Ohtori, S.; Moriya, H.; Takahashi, K. Distribution and immunocytochemical characterization of dorsal root ganglion neurons innervating the lumbar intervertebral disc in rats: a review. *Life sciences* **2004**, *74*, 2627−42.
(18) Groh, A. M. R.; Fournier, D. E.; Battié, M. C.; Séguin, C. A. Innervation of the Human Intervertebral Disc: A Scoping Review. *Pain medicine (Malden, Mass.)* **2021**, *22* (6), 1281−1304.
(19) Nakawaki, M.; Uchida, K.; Miyagi, M.; Inoue, G.; Kawakubo, A.; Satoh, M.; Takaso, M. Changes in Nerve Growth Factor Expression and Macrophage Phenotype Following Intervertebral Disc Injury in Mice. *Journal of orthopaedic research: official publication of the Orthopaedic Research Society* **2019**, *37*, 1798−1804.
(20) Takahashi, K.; Aoki, Y.; Ohtori, S. Resolving discogenic pain. *European spine journal: official publication of the European Spine Society, the European Spinal Deformity Society, and the European Section of the Cervical Spine Research Society* **2008**, *17*, 428−431.
(21) Liu, C.; Hu, F.; Jiao, G.; Guo, Y.; Zhou, P.; Zhang, Y.; Zhang, Z.; Yi, J.; You, Y.; Li, Z.; Wang, H.; Zhang, X. Dental pulp stem cell-derived exosomes suppress M1 macrophage polarization through the ROS-MAPK-NFκB P65 signaling pathway after spinal cord injury. *J. Nanobiotechnol.* **2022**, *20* (1), 65.
(22) Wang, D. K.; Zheng, H. L.; Zhou, W. S.; Duan, Z. W.; Jiang, S. D.; Li, B.; Zheng, X. F.; Jiang, L. S. Mitochondrial Dysfunction in Oxidative Stress-Mediated Intervertebral Disc Degeneration. *Orthopaedic surgery* **2022**, *14*, 1569−1582.
(23) De Santa, F.; Vitiello, L.; Torcinaro, A.; Ferraro, E. The Role of Metabolic Remodeling in Macrophage Polarization and Its Effect on Skeletal Muscle Regeneration. *Antioxidants & redox signaling* **2019**, *30*, 1553−1598.
(24) Wang, L.; Zhu, B.; Deng, Y.; Li, T.; Tian, Q.; Yuan, Z.; Ma, L.; Cheng, C.; Guo, Q.; Qiu, L. Biocatalytic and Antioxidant Nanostructures for ROS Scavenging and Biotherapeutics. *Adv. Funct. Mater.* **2021**, *31*, 2101804.
(25) Chen, L.; Tiwari, S. R.; Zhang, Y.; Zhang, J.; Sun, Y. Facile Synthesis of Hollow MnO(2) Nanoparticles for Reactive Oxygen Species Scavenging in Osteoarthritis. *ACS biomaterials science & engineering* **2021**, *7*, 1686−1692.
(26) Huang, Y.; Liu, Z.; Liu, C.; Ju, E.; Zhang, Y.; Ren, J.; Qu, X. Self-Assembly of Multi-nanozymes to Mimic an Intracellular Antioxidant Defense System. *Angewandte Chemie (International ed. in English)* **2016**, *55*, 6646−50.
(27) Luk, B. T.; Zhang, L. Cell membrane-camouflaged nanoparticles for drug delivery. *Journal of controlled release: official journal of the Controlled Release Society* **2015**, *220*, 600−7.
(28) Chen, H. Y.; Deng, J.; Wang, Y.; Wu, C. Q.; Li, X.; Dai, H. W. Hybrid cell membrane-coated nanoparticles: A multifunctional biomimetic platform for cancer diagnosis and therapy. *Acta biomaterialia* **2020**, *112*, 1−13.
(29) Chen, Z.; Zhao, P.; Luo, Z.; Zheng, M.; Tian, H.; Gong, P.; Gao, G.; Pan, H.; Liu, L.; Ma, A.; Cui, H.; Ma, Y.; Cai, L. Cancer Cell Membrane-Biomimetic Nanoparticles for Homologous-Targeting Dual-Modal Imaging and Photothermal Therapy. *ACS Nano* **2016**, *10*, 10049−10057.
(30) Zhou, M.; Aziz, M.; Denning, N. L.; Yen, H. T.; Ma, G.; Wang, P. Extracellular CIRP induces macrophage endotoxin tolerance through IL-6R-mediated STAT3 activation. *JCI insight* **2020**, *5* (5), e133715.
(31) Lübow, C.; Bockstiegel, J.; Weindl, G. Lysosomotropic drugs enhance pro-inflammatory responses to IL-1β in macrophages by inhibiting internalization of the IL-1 receptor. *Biochemical pharmacology* **2020**, *175*, 113864.
(32) Coyne, C.; Baravick, J.; Howell, T., 3rd; Baravick, E.; Willetto, C.; Fenwick, B. W. Biochemical mechanisms that interact with membrane-associated IL-1 RII (60-kDa decoy) receptors in populations of adherent macrophages and vascular endothelium. *Cellular signalling* **2001**, *13* (10), 765−76.
(33) Thamphiwatana, S.; Angsantikul, P.; Escajadillo, T.; Zhang, Q.; Olson, J.; Luk, B. T.; Zhang, S.; Fang, R. H.; Gao, W.; Nizet, V.; Zhang, L. Macrophage-like nanoparticles concurrently absorbing endotoxins and proinflammatory cytokines for sepsis management. *Proc. Natl. Acad. Sci. U.S.A.* **2017**, *114*, 11488−11493.
(34) Hirose, M.; Kuroda, Y.; Murata, E. NGF/TrkA Signaling as a Therapeutic Target for Pain. *Pain practice: the official journal of World Institute of Pain* **2016**, *16*, 175−82.
(35) Zabeti, M.; Wan Daud, W. M. A.; Aroua, M. K. Activity of solid catalysts for biodiesel production: A review. *Fuel Process. Technol.* **2009**, *90* (6), 770−777.
(36) Chen, P.; Liu, X.; Gu, C.; Zhong, P.; Song, N.; Li, M.; Dai, Z.; Fang, X.; Liu, Z.; Zhang, J.; Tang, R.; Fan, S.; Lin, X. A plant-derived natural photosynthetic system for improving cell anabolism. *Nature* **2022**, *612*, 546−554.
(37) Xiong, J.; Wu, M.; Chen, J.; Liu, Y.; Chen, Y.; Fan, G.; Liu, Y.; Cheng, J.; Wang, Z.; Wang, S.; Liu, Y.; Zhang, W. Cancer-Erythrocyte Hybrid Membrane-Camouflaged Magnetic Nanoparticles with Enhanced Photothermal-Immunotherapy for Ovarian Cancer. *ACS Nano* **2021**, *15*, 19756−19770.
(38) Yang, G.; Liao, W.; Shen, M.; Mei, H. Insight into neural mechanisms underlying discogenic back pain. *Journal of international medical research* **2018**, *46*, 4427−4436.
(39) Mosley, G. E.; Wang, M.; Nasser, P.; Lai, A.; Charen, D. A.; Zhang, B.; Iatridis, J. C. Males and females exhibit distinct relationships between intervertebral disc degeneration and pain in a rat model. *Sci. Rep.* **2020**, *10*, 15120.
(40) Gaudet, A. D.; Fonken, L. K.; Ayala, M. T.; Maier, S. F.; Watkins, L. R. Aging and miR-155 in mice influence survival and neuropathic pain after spinal cord injury. *Brain, behavior, and immunity* **2021**, *97*, 365−370.
(41) Yoshimura, Y.; Nakamura, K.; Seno, M.; Mochizuki, M.; Kawai, K.; Koba, S.; Watanabe, T. Generation of c-Fos knockout rats, and observation of their phenotype. *Experimental animals* **2023**, *72*, 95−102.
(42) Ikeshima-Kataoka, H.; Matsui, Y.; Uede, T. Osteopontin is indispensable for activation of astrocytes in injured mouse brain and primary culture. *Neurological research* **2018**, *40*, 1071−1079.
(43) Lyu, F. J.; Cui, H.; Pan, H.; Mc Cheung, K.; Cao, X.; Iatridis, J. C.; Zheng, Z. Painful intervertebral disc degeneration and inflammation: from laboratory evidence to clinical interventions. *Bone research* **2021**, *9*, 7.
(44) Song, C.; Zhou, Y.; Cheng, K.; Liu, F.; Cai, W.; Zhou, D.; Chen, R.; Shi, H.; Fu, Z.; Chen, J.; Liu, Z. Cellular senescence - Molecular mechanisms of intervertebral disc degeneration from an immune perspective. *Biomedecine & pharmacotherapie* **2023**, *162*, 114711.
(45) Zhang, Y.; He, F.; Chen, Z.; Su, Q.; Yan, M.; Zhang, Q.; Tan, J.; Qian, L.; Han, Y. Melatonin modulates IL-1β-induced extracellular matrix remodeling in human nucleus pulposus cells and attenuates rat intervertebral disc degeneration and inflammation. *Aging* **2019**, *11*, 10499−10512.
(46) He, X.; Qian, Y.; Li, Z.; Fan, E. K.; Li, Y.; Wu, L.; Billiar, T. R.; Wilson, M. A.; Shi, X.; Fan, J. TLR4-Upregulated IL-1β and IL-1RI Promote Alveolar Macrophage Pyroptosis and Lung Inflammation through an Autocrine Mechanism. *Sci. Rep.* **2016**, *6*, 31663.
(47) Xu, X.; Xu, J.; Wu, J.; Hu, Y.; Han, Y.; Gu, Y.; Zhao, K.; Zhang, Q.; Liu, X.; Liu, J.; Liu, B.; Cao, X. Phosphorylation-Mediated IFN-γR2Membrane Translocation Is Required to Activate Macrophage Innate Response. *Cell* **2018**, *175*, 1336−1351 e17.
(48) Wajant, H.; Siegmund, D. TNFR1 and TNFR2 in the Control of the Life and Death Balance of Macrophages. *Frontiers in cell and developmental biology* **2019**, *7*, 91.
(49) Shi, M.; Shen, K.; Yang, B.; Zhang, P.; Lv, K.; Qi, H.; Wang, Y.; Li, M.; Yuan, Q.; Zhang, Y. An electroporation strategy to synthesize the membrane-coated nanoparticles for enhanced anti-inflammation therapy in bone infection. *Theranostics* **2021**, *11* (5), 2349−2363.
(50) Viola, A.; Munari, F.; Sánchez-Rodríguez, R.; Scolaro, T.; Castegna, A. The Metabolic Signature of Macrophage Responses. *Frontiers in immunology* **2019**, *10*, 1462.

https://doi.org/10.1021/acsnano.3c08097
ACS Nano 2024, 18, 3053−3072

(51) Qian, J.; Wang, X.; Su, G.; Shu, X.; Huang, Z.; Jiang, H.; Zhu, Q. Platelet-rich plasma-derived exosomes attenuate intervertebral disc degeneration by promoting NLRP3 autophagic degradation in macrophages. *International immunopharmacology* **2022**, *110*, 108962.
(52) Teng, Y.; Huang, Y.; Yu, H.; Wu, C.; Yan, Q.; Wang, Y.; Yang, M.; Xie, H.; Wu, T.; Yang, H.; Zou, J. Nimbolide targeting SIRT1 mitigates intervertebral disc degeneration by reprogramming cholesterol metabolism and inhibiting inflammatory signaling. *Acta pharmaceutica Sinica. B* **2023**, *13*, 2269−2280.
(53) An, Y.; Zhang, H.; Wang, C.; Jiao, F.; Xu, H.; Wang, X.; Luan, W.; Ma, F.; Ni, L.; Tang, X.; Liu, M.; Guo, W.; Yu, L. Activation of ROS/MAPKs/NF-κB/NLRP3 and inhibition of efferocytosis in osteoclast-mediated diabetic osteoporosis. *FASEB journal: official publication of the Federation of American Societies for Experimental Biology* **2019**, *33*, 12515−12527.
(54) Zhang, H. J.; Liao, H. Y.; Bai, D. Y.; Wang, Z. Q.; Xie, X. W. MAPK /ERK signaling pathway: A potential target for the treatment of intervertebral disc degeneration. *Biomedecine & pharmacotherapie* **2021**, *143*, 112170.
(55) Zhang, G. Z.; Deng, Y. J.; Xie, Q. Q.; Ren, E. H.; Ma, Z. J.; He, X. G.; Gao, Y. C.; Kang, X. W. Sirtuins and intervertebral disc degeneration: Roles in inflammation, oxidative stress, and mitochondrial function. *Clinica chimica acta; international journal of clinical chemistry* **2020**, *508*, 33−42.
(56) Mittal, M.; Siddiqui, M. R.; Tran, K.; Reddy, S. P.; Malik, A. B. Reactive oxygen species in inflammation and tissue injury. *Antioxidants & redox signaling* **2014**, *20*, 1126−67.
(57) Ye, H.; Ma, Z.; Liu, L.; Zhang, T.; Han, Q.; Xiang, Z.; Xia, Y.; Ke, Y.; Guan, X.; Shi, Q.; Ataullakhanov, F. I.; Panteleev, M. Thrombus Inhibition and Neuroprotection for Ischemic Stroke Treatment through Platelet Regulation and ROS Scavenging. *ChemMedChem.* **2022**, *17*, No. e202200317.
(58) Yang, B.; Chen, Y.; Shi, J. Reactive Oxygen Species (ROS)-Based Nanomedicine. *Chem. Rev.* **2019**, *119* (8), 4881−4985.
(59) Li, L.; Tan, J.; Miao, Y.; Lei, P.; Zhang, Q. ROS and Autophagy: Interactions and Molecular Regulatory Mechanisms. *Cellular and molecular neurobiology* **2015**, *35*, 615−21.
(60) Morgan, M. J.; Liu, Z. G. Crosstalk of reactive oxygen species and NF-κB signaling. *Cell research* **2011**, *21*, 103−15.
(61) Srinivas, U. S.; Tan, B. W. Q.; Vellayappan, B. A.; Jeyasekharan, A. D. ROS and the DNA damage response in cancer. *Redox biology* **2019**, *25*, 101084.
(62) Rendra, E.; Riabov, V.; Mossel, D. M.; Sevastyanova, T.; Harmsen, M. C.; Kzhyshkowska, J. Reactive oxygen species (ROS) in macrophage activation and function in diabetes. *Immunobiology* **2019**, *224*, 242−253.
(63) Yang, Q.; Jiang, H.; Wang, Y.; Leng, X.; Wang, Y.; Tong, J.; Zhou, Y.; Mo, C.; Peng, J.; Gao, H. Plaque Macrophage-Targeting Nanosystems with Cooperative Co-Regulation of ROS and TRAF6 for Stabilization of Atherosclerotic Plaques. *Adv. Funct. Mater.* **2023**, *33* (28), 2301053.
(64) Rao, L.; Yu, G.-T.; Meng, Q.-F.; Bu, L.-L.; Tian, R.; Lin, L.-S.; Deng, H.; Yang, W.; Zan, M.; Ding, J.; Li, A.; Xiao, H.; Sun, Z.-J.; Liu, W.; Chen, X. Cancer Cell Membrane-Coated Nanoparticles for Personalized Therapy in Patient-Derived Xenograft Models. *Adv. Funct. Mater.* **2019**, *29* (51), 1905671.
(65) Peng, Y.; Chen, X.; Rao, Z.; Wu, W.; Zuo, H.; Chen, K.; Li, K.; Lin, H.; Liu, S.; Xiao, Y.; Wang, B.; Quan, D.; Qing, X.; Bai, Y.; Shao, Z. Multifunctional annulus fibrosus matrix prevents disc-related pain via inhibiting neuroinflammation and sensitization. *Acta biomaterialia* **2023**, *170*, 288.
(66) Risbud, M. V.; Shapiro, I. M. Role of cytokines in intervertebral disc degeneration: pain and disc content. *Nature reviews. Rheumatology* **2014**, *10*, 44−56.
(67) Wang, Y.; Che, M.; Xin, J.; Zheng, Z.; Li, J.; Zhang, S. The role of IL-1β and TNF-α in intervertebral disc degeneration. *Biomedecine & pharmacotherapie* **2020**, *131*, 110660.
(68) Purmessur, D.; Freemont, A. J.; Hoyland, J. A. Expression and regulation of neurotrophins in the nondegenerate and degenerate human intervertebral disc. *Arthritis research & therapy* **2008**, *10*, R99.
(69) Reed, N. R.; Reed, W. R.; Syrett, M.; Richey, M. L.; Frolov, A.; Little, J. W. Somatosensory behavioral alterations in a NGF-induced persistent low back pain model. *Behavioural brain research* **2022**, *418*, 113617.
(70) Daraee, H.; Etemadi, A.; Kouhi, M.; Alimirzalu, S.; Akbarzadeh, A. Application of liposomes in medicine and drug delivery. *Artificial cells, nanomedicine, and biotechnology* **2016**, *44*, 381−91.
(71) Fang, R. H.; Gao, W.; Zhang, L. Targeting drugs to tumours using cell membrane-coated nanoparticles. *Nature reviews. Clinical oncology* **2023**, *20*, 33−48.
(72) Fu, Y.; He, G.; Liu, Z.; Wang, J.; Li, M.; Zhang, Z.; Bao, Q.; Wen, J.; Zhu, X.; Zhang, C.; Zhang, W. DNA Base Pairing-Inspired Supramolecular Nanodrug Camouflaged by Cancer-Cell Membrane for Osteosarcoma Treatment. *Small (Weinheim an der Bergstrasse, Germany)* **2022**, *18*, No. e2202337.
(73) Pan, T.; Deng, H.; Kang, S.; Zhang, Y.; Lian, W.; Zhang, C.; He, H. Facile homogeneous precipitation method to prepare MnO2 with high performance in catalytic oxidation of ethyl acetate. *Chemical Engineering Journal* **2021**, *417*, 129246.
(74) Li, C.; Zhao, Z.; Luo, Y.; Ning, T.; Liu, P.; Chen, Q.; Chu, Y.; Guo, Q.; Zhang, Y.; Zhou, W.; Chen, H.; Zhou, Z.; Wang, Y.; Su, B.; You, H.; Zhang, T.; Li, X.; Song, H.; Li, C.; Sun, T.; Jiang, C. Macrophage-Disguised Manganese Dioxide Nanoparticles for Neuroprotection by Reducing Oxidative Stress and Modulating Inflammatory Microenvironment in Acute Ischemic Stroke. *Advanced science (Weinheim, Baden-Wurttemberg, Germany)* **2021**, *8* (20), No. e2101526.
(75) Wu, W.; Jing, D.; Huang, X.; Yang, W.; Shao, Z. Drp1-mediated mitochondrial fission is involved in oxidized low-density lipoprotein-induced AF cella poptosis. *Journal of orthopaedic research: official publication of the Orthopaedic Research Society* **2021**, *39*, 1496−1504.
(76) Lin, H.; Peng, Y.; Li, J.; Wang, Z.; Chen, S.; Qing, X.; Pu, F.; Lei, M.; Shao, Z. Reactive Oxygen Species Regulate Endoplasmic Reticulum Stress and ER-Mitochondrial Ca(2+) Crosstalk to Promote Programmed Necrosis of Rat Nucleus Pulposus Cells under Compression. *Oxidative medicine and cellular longevity* **2021**, *2021*, 8810698.
(77) Peng, Y.; Qing, X.; Lin, H.; Huang, D.; Li, J.; Tian, S.; Liu, S.; Lv, X.; Ma, K.; Li, R.; Rao, Z.; Bai, Y.; Chen, S.; Lei, M.; Quan, D.; Shao, Z. Decellularized Disc Hydrogels for hBMSCs tissue-specific differentiation and tissue regeneration. *Bioactive materials* **2021**, *6*, 3541−3556.

NOTE ADDED AFTER ASAP PUBLICATION

This paper was published ASAP on January 18, 2024, with a duplicate reference. The corrected version was reposted on January 22, 2024.

https://doi.org/10.1021/acsnano.3c08097
ACS Nano 2024, 18, 3053−3072